Tympel, Saskia; Boeck, Thomas; Schumacher, Jörg:

Laminar and transitional liquid metal duct flow near a magnetic point dipole

URN: urn:nbn:de:gbv:ilm1-2015210122

Published OpenAccess: January 2015

Original published in:

Journal of fluid mechanics. - Cambridge [u.a.] : Cambridge Univ. Press (ISSN 1469-7645). - 735 (2013), S. 553-586.
DOI: 10.1017/jfm.2013.491
URL: http://dx.doi.org/10.1017/jfm.2013.491
[Visited: 2014-08-27]

J. Fluid Mech. (2013), *vol.* 735, *pp.* 553–586.
doi:10.1017/jfm.2013.491

Laminar and transitional liquid metal duct flow near a magnetic point dipole

Saskia Tympel†, Thomas Boeck and Jörg Schumacher

Institut für Thermo- und Fluiddynamik, Technische Universität Ilmenau, Postfach 100565, D-98684 Ilmenau, Germany

(Received 23 January 2013; revised 30 August 2013; accepted 12 September 2013; first published online 28 October 2013)

The flow transformation and the generation of vortex structures by a strong magnetic dipole field in a liquid metal duct flow is studied by means of three-dimensional direct numerical simulations. The dipole is considered as the paradigm for a magnetic obstacle which will deviate the streamlines due to Lorentz forces acting on the fluid elements. The duct is of square cross-section. The dipole is located above the top wall and is centred in spanwise direction. Our model uses the quasistatic approximation which is applicable in the limit of small magnetic Reynolds numbers. The analysis covers the stationary flow regime at small hydrodynamic Reynolds numbers Re as well as the transitional time-dependent regime at higher values which may generate a turbulent flow in the wake of the magnetic obstacle. We present a systematic study of these two basic flow regimes and their dependence on Re and on the Hartmann number Ha, a measure of the strength of the magnetic dipole field. Furthermore, three orientations of the dipole are compared: streamwise-, spanwise- and wall-normal-oriented dipole axes. The most efficient generation of turbulence at a fixed distance above the duct follows for the spanwise orientation, which is caused by a certain configuration of Hartmann layers and reversed flow at the top plate. The enstrophy in the turbulent wake grows linearly with Ha which is connected with a dominance of the wall-normal derivative of the streamwise velocity.

Key words: MHD and electrohydrodynamics, transition to turbulence, vortex shedding

1. Introduction

Fluid motion which is interacting with electromagnetic fields plays a central role for the dynamics in the interior and atmospheres of stars (Biskamp 1993; Rüdiger & Hollerbach 2004) or in nuclear fusion (Niu 1989). Although less spectacular, such interactions also occur in flows of molten metals in technological applications ranging from the generation of monocrystals for silicon wafers to the production of steel and complex alloys for industrial manufacturing (Davidson 1999). Understanding the basic mechanisms of how an electromagnetic field generates or suppresses fluid motion is a prerequisite for the efficient electromagnetic control of such technological processes. Applying this knowledge may for example improve the purity of the materials.

Apart from flow control, electromagnetic fields can also be employed for flow measurement in conducting liquids. Inductive flow meters determine the fluid velocity

† Email address for correspondence: saskia.tympel@tu-ilmenau.de

from the voltage induced across the flow as it traverses a magnetic field (Shercliff 1962). This method is well-established and very accurate. However, it is not contactless but requires electrodes in the liquid. It is therefore not suited for hot and aggressive molten metals. Several efforts of the last decade have, therefore, been devoted to the development of contactless methods for such non-transparent liquids based on electromagnetic induction. Examples of such methods are the contactless inductive flow tomography (Stefani, Gundrum & Gerbeth 2004), the rotary flow meter (Priede, Buchenau & Gerbeth 2011) and Lorentz force velocimetry (LFV) (Thess, Votyakov & Kolesnikov 2006; Thess *et al.* 2007).

In LFV, the currents which are induced in the flow by an external magnet system result in a braking force on the flow. Conversely, the flow exerts a reaction force on the magnet on account of Newton's third law. This Lorentz force on the magnet depends on the velocity magnitude and distribution, and can be used for velocity measurement. The state of the art in LFV is largely limited to global measurements, i.e. mean velocities or volume fluxes of the liquid metal flow. The utility of LFV for local measurement has been demonstrated only very recently for the wake behind a solid obstacle (Heinicke 2013). It requires a localized field that pervades only a small portion of the flow domain, where the flow can be significantly modified by the Lorentz force. Further development of LFV for detailed, spatially resolved measurements requires a better understanding of such aspects. They have to be studied by direct numerical simulations (DNS) since only DNS can provide the fully resolved space–time evolution of three-dimensional liquid metal flows and Lorentz force components that affect the motion. By means of DNS, the local impact of the magnetic field and the related parameter dependencies can be studied systematically in laminar, transient or turbulent cases. Owing the high computational cost of DNS, this approach will remain limited to a moderate range of dimensionless parameters, i.e. Reynolds and Hartmann numbers, Re and Ha.

In recent years, computations of liquid-metal magnetohydrodynamic (MHD) flows have become more frequent, and a number of DNS studies have been reported. Typically, such works were concerned with effects arising from the anisotropic nature of the Joule damping and from the specific MHD boundary layers at walls (Boeck, Krasnov & Zienicke 2007; Knaepen & Moreau 2008; Vantieghem, Albets-Chico & Knaepen 2009; Chaudhary, Vanka & Thomas 2010; Krasnov *et al.* 2010; Krasnov, Zikanov & Boeck 2012; Zhao & Zikanov 2012). Instabilities of MHD boundary layers such as the Hartmann layer, and the transition to turbulence have been analysed numerically in ducts and channels for homogeneous magnetic fields (Gerard-Varet 2002; Airiau & Castets 2004; Krasnov *et al.* 2004; Kobayashi 2008; Shatrov & Gerbeth 2010; Krasnov *et al.* 2013). From the LFV perspective, such investigations are of limited interest because the total Lorentz force vanishes in the case of a homogeneous field.

The aim of this article is to investigate the structure formation and the locally resolved Lorentz force fields in a liquid metal duct flow in the presence of a magnetic point dipole field. The flow and magnetic field configurations are similar to recent laboratory experiments on LFV using liquid InGaSn alloy at room temperature (Heinicke *et al.* 2012). We conduct three-dimensional DNS based on the quasistatic approximation of the induction equation. This approximation applies for liquid metal flows with a high conductivity which are considered here and can be found typically in laboratory experiments and industrial applications (Davidson 2006). The induced magnetic field is then weak and does not modify the stronger primary magnetic field significantly. Hence, the induced currents depend linearly on the velocity field and

can be computed from Ohm's law for a moving conductor with the electric field represented by a potential gradient.

In terms of the flow geometry, we will focus on a straight duct flow with square cross-section as one of the simplest shear flow configurations. Our choice of a magnetic dipole field is also guided by mathematical simplicity and by its rapid decay. A drawback is that it represents the far field of a typical permanent magnet, i.e. it will not provide a very good approximation when such a magnet is placed close to the duct (Heinicke *et al.* 2012). Owing to its rapid decay, the MHD interaction of the dipole field with the flow is strongly localized and three-dimensional. We will demonstrate that it can cause a locally pronounced deflection of the velocity field for laminar flows, and that the wake of the dipole is characterized by vortical structures at higher velocities. For particular orientations of the magnetic dipole moment, transition to turbulence in the wake is observed at moderate Reynolds numbers. In order to keep the parameter space manageable we only consider three basic orientations of the magnetic dipole moment, namely along the streamwise, spanwise and wall-normal directions.

The present study can be regarded as a continuation of the theoretical and numerical investigations reported in Heinicke *et al.* (2012). In this previous work, dynamic effects of the Lorentz force on the flow were only significant in the creeping flow regime. As before, we shall not only consider the flow modification but also determine the electromagnetic force and torque on the dipole, which are of great interest from the perspective of LFV.

Without reference to LFV, the flow modification by a localized magnetic field has also been investigated by other authors. Cuevas, Smolentsev & Abdou (2006*a*) have termed it a magnetic obstacle in analogy with the flow around a solid obstacle. Similar configurations have been investigated both experimentally and numerically (Andreev, Kolesnikov & Thess 2006; Votyakov *et al.* 2007; Votyakov, Zienicke & Kolesnikov 2008; Andreev, Kolesnikov & Thess 2009; Kenjeres 2012). The magnetic fields in these works typically had a lower degree of spatial non-uniformity, and cannot be characterized in such as simple way as a point dipole. A point dipole has been used for analytic investigations in Cuevas, Smolentsev & Abdou (2006*b*), but for a quasi-two-dimensional problem. In addition, force and torque on the magnet system were typically also not studied, and three-dimensional simulations were performed with relatively coarse grids (e.g. Votyakov *et al.* 2008). We therefore also attempt to significantly improve on these earlier works in terms of numerical resolution.

Naturally, the geometric parameters, such as position and orientation of the magnetic dipole, have a strong influence on the acting forces. However, a detailed investigation of this point would go beyond the scope of this article. Indeed, we will focus on the influence of the hydrodynamic Reynolds number Re and the Hartmann number Ha. In brief, the Reynolds number describes the ratio of the inertial to the viscous forces in the flow (mathematical definitions of both numbers will be given in (2.4) and (2.5)). The Hartmann number is a measure for the strength of the magnetic field and its influence on the flow. Both parameters are investigated in a wide range, as displayed in figure 1. Since it is understood that the position of the dipole is important for the spatial development and transformation of the flow, we consider two particular distances between dipole and duct. In particular, a very short distance is used for the lower Reynolds numbers, as this allows a direct comparison with recent laboratory experiments by Heinicke *et al.* (2012). At higher Reynolds numbers the magnetic dipole is positioned further away from the top wall of the duct. This changes the

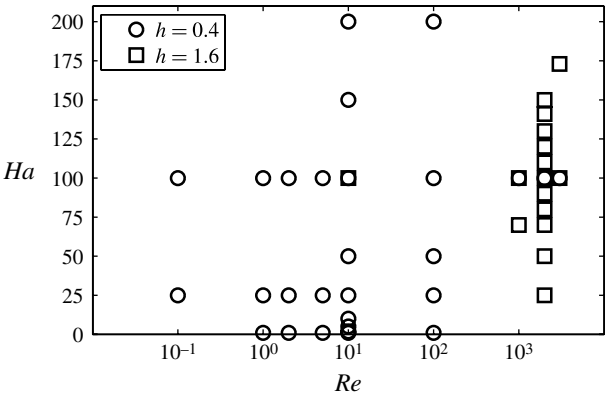

FIGURE 1. Parameter sets of the Hartmann and Reynolds numbers, *Ha* and *Re*, investigated. Each point denotes a separate DNS. The distances h of the dipole from the top surface of the duct is $h = 0.4$ (circles) or $h = 1.6$ (squares) measured in units of the half-width of the duct.

magnetic field configuration inside the flow and excites vortices that will eventually cause the flow to become turbulent.

The article is organized as follows. First, we introduce the geometry and setting of the problem under consideration in § 2.1 and explain the numerical method in § 2.2. Second, we present the results for low Reynolds number to describe the basic deformations of the flow field in § 3 in the stationary regime. This regime exists for the lower Reynolds numbers and persists when both, *Ha* and *Re*, are increased to a certain point. In § 4, we discuss the transition to turbulence when the Reynolds number is further increased. Conclusions and a brief outlook are given in § 5.

2. Definition of the problem

2.1. *Equations of motion and set-up*

We consider the flow of an electrically conducting fluid in a square duct of side length $2L$, i.e. the characteristic length L will be defined as the half-width of the duct. We use Cartesian coordinates, where the streamwise direction is denoted as x, the spanwise direction as y and the vertical, wall-normal direction as z. The duct is exposed to the inhomogeneous magnetic field of a point dipole located at a vertical distance H above the top surface of the duct. In dimensional units, the dipole field at position $\boldsymbol{x}$ is given by (Jackson 1998)

$$\boldsymbol{B} = \frac{\mu_0 M}{4\pi}\left(\frac{3\boldsymbol{m}\cdot\boldsymbol{r}}{|\boldsymbol{r}|^5}\boldsymbol{r} - \frac{\boldsymbol{m}}{|\boldsymbol{r}|^3}\right), \tag{2.1}$$

where M denotes the magnetic dipole moment and the unit vector $\boldsymbol{m}$ its orientation. The other quantities are the vacuum permeability μ_0 and the distance $\boldsymbol{r} = \boldsymbol{x} - \boldsymbol{r}_0$ between $\boldsymbol{x}$ and the dipole position at $\boldsymbol{r}_0$. For non-dimensionalization of the problem we use the maximum value

$$B_{max} = \frac{\mu_0 M}{4\pi H^3}\sqrt{m_x^2 + m_y^2 + 4m_z^2} \tag{2.2}$$

of the dipole field within the duct as unit of magnetic induction.

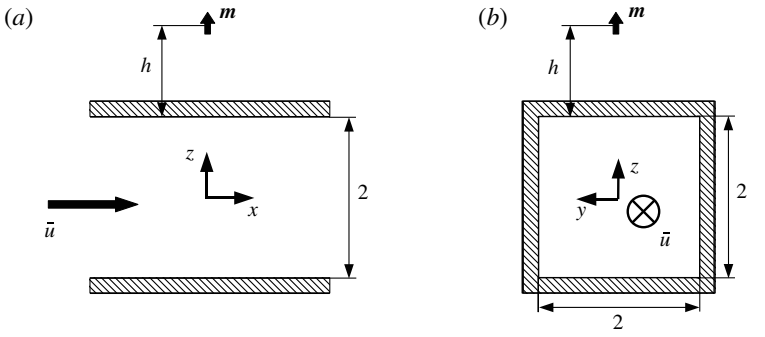

FIGURE 2. Set-up of the problem. (*a*) Side view. (*b*) Rear view. The mean velocity $\bar{u}$ of the duct flow points in the positive x direction. The origin of the coordinate system is placed at the centre of the duct. The distance between magnetic point dipole and fluid surface is denoted as h. The characteristic length scale of this set-up is chosen to be the half-width of the duct. All lengths are expressed in this unit.

Based on B_{max} and L as the unit of length, the non-dimensional magnetic flux density of the dipole is

$$\boldsymbol{B}'(\boldsymbol{x}') = \frac{h^3}{\sqrt{m_x^2 + m_y^2 + 4m_z^2}} \left(\frac{3\boldsymbol{m} \cdot \boldsymbol{r}'}{|\boldsymbol{r}'|^5} \boldsymbol{r}' - \frac{\boldsymbol{m}}{|\boldsymbol{r}'|^3} \right), \tag{2.3}$$

where $h = H/L$ is the non-dimensional distance between the dipole and duct and non-dimensional quantities are indicated by a prime. In the following, we shall use non-dimensional quantities exclusively and will therefore omit the prime in subsequent equations.

A sketch of the set-up in dimensionless units is shown in figure 2. The origin is chosen to be at the centreline of the duct. Thus, the duct extends in the y and z directions from -1 to 1. The position of the dipole is given by $\boldsymbol{r}_0 = (0, 0, h + 1)$, i.e. in the vertical centre plane. A key parameter of our study is the orientation of the magnetic moment of the point dipole, which is referred to as the dipole orientation. We will call the orientation streamwise if $\boldsymbol{m} = \boldsymbol{e}_x$, spanwise if $\boldsymbol{m} = \boldsymbol{e}_y$ and vertical if $\boldsymbol{m} = \boldsymbol{e}_z$. In this article, we only consider these three main orientations, but preliminary studies have shown that oblique orientations lead to more complex structures in the flow which will be discussed elsewhere.

As mentioned above, the dipole field approximates the far field of a small permanent magnet. Close to the permanent magnet the dipole is not a very accurate model for the actual field. Nevertheless, the differences are not substantial. We have measured the field distribution around a cube magnet of 1 cm side length and compared it with a point dipole. The dipole moment was chosen such that the magnetic induction agrees between the cube magnet and the dipole at 1 cm distance from its centre. The magnetic induction was compared along the dipole axis for distances greater than 1 cm. At identical positions, the relative error in magnetic induction between dipole and cube magnet never exceeded 30 %. Details can be found in Tympel (2013).

Before listing the equations that will be solved numerically, we want to recall the basic physical principle which causes the deflection of the fluid motion. Inside the square duct, there is a laminar pressure-driven flow of an electrically conducting liquid. The magnetic dipole close to the duct induces electric currents, which are confined to

the flow due to the insulating walls. These currents give rise to two effects. First, they induce a secondary magnetic field. This secondary magnetic field will be much weaker than the primary field of the point dipole. In many applications in metallurgy, one may assume that the secondary magnetic field is negligible. This idea coincides with the assumption that the *magnetic* Reynolds number *Rm* (Moreau 1990; Davidson 2006) is very small. Therefore, we can neglect the secondary field and apply the quasistatic approximation. Physically, this means that the flow is unable to deform the field lines of the magnetic dipole. There is no feedback from the flow onto the magnetic field.

Second, the currents induced by the primary magnetic field of the dipole generate a Lorentz force within the liquid. It gives rise to a strong deformation of the velocity profiles (cf. § 3) and even triggers a transition to turbulence (cf. § 4). Owing to Newton's third law, a counter force acts on the magnetic dipole which is of same magnitude, but of opposite sign as the total force $\boldsymbol{F}$ on the liquid. Recent works by Heinicke *et al.* (2012) were focused on the determination of this force and the derivation of mean flow properties from its magnitude. Here, we will focus on the particular impact of the Lorentz force on the local velocity field and the resulting flow transformation.

In addition to the geometry parameters, the problem depends on two dimensionless parameters *Re* and *Ha*. The Reynolds number *Re* is defined as

$$Re \equiv \frac{\bar{u}L}{\nu}, \tag{2.4}$$

where $\bar{u}$ is the mean streamwise velocity and ν the kinematic viscosity. The strength of the magnetic field is quantified by the Hartmann number

$$Ha \equiv B_{max} L \sqrt{\frac{\sigma}{\rho \nu}}, \tag{2.5}$$

where ρ is the mass density and σ the electric conductivity. In contrast to the case of a uniform magnetic field, the definition of *Ha* in the present case is ambiguous because of the non-uniform magnetic flux density. We choose the maximum of the magnetic flux density B_{max} inside the duct. It occurs at the upper boundary of the duct right below the dipole at point $x = y = 0$ and $z = 1$.

The governing equations of the problem will be given in non-dimensional form below. We use $\bar{u}$ as the unit of velocity and L as the unit of length. The pressure, electric current density and potential are given in units of $\rho\bar{u}^2$, $\sigma\bar{u}B_{max}$ and $\bar{u}B_{max}L$, respectively. To model the interaction between the Lorentz force $\boldsymbol{f}$ and the conducting liquid, we solve the incompressible Navier–Stokes equations

$$\partial_t \boldsymbol{u} + (\boldsymbol{u} \cdot \boldsymbol{\nabla})\boldsymbol{u} = -\boldsymbol{\nabla} p + \frac{1}{Re}\nabla^2 \boldsymbol{u} + \boldsymbol{f}, \tag{2.6}$$

$$\boldsymbol{f} = \frac{Ha^2}{Re}\boldsymbol{j} \times \boldsymbol{B}, \tag{2.7}$$

$$\boldsymbol{\nabla} \cdot \boldsymbol{u} = 0. \tag{2.8}$$

The induced currents are given by Ohm's law

$$\boldsymbol{j} = -\boldsymbol{\nabla}\phi + \boldsymbol{u} \times \boldsymbol{B}, \tag{2.9}$$

where the electric field is represented by the negative gradient of the electric potential ϕ. It is determined by the condition $\boldsymbol{\nabla} \cdot \boldsymbol{j} = 0$, which corresponds to the Poisson

equation

$$\Delta\phi = \nabla \cdot (\boldsymbol{u} \times \boldsymbol{B}). \tag{2.10}$$

Equations (2.9) and (2.10) constitute the quasistatic approximation (Davidson 2006) with an imposed field $\boldsymbol{B}$. For the velocity, we use no-slip boundary conditions, i.e.

$$\boldsymbol{u} = 0 \tag{2.11}$$

at all walls. Furthermore, all walls are insulating with zero wall-normal currents, and we therefore apply

$$\frac{\partial\phi}{\partial\boldsymbol{n}} = 0, \tag{2.12}$$

where $\boldsymbol{n}$ denotes the corresponding normal direction perpendicular to the walls. In the streamwise direction, we apply the periodic boundary condition in our simulations. For higher Reynolds numbers, we model inflow and outflow conditions with the help of the so-called fringe force as described below in § 2.2.

2.2. *Numerical method using a fringe force*

Our DNS are performed using the code from Krasnov, Zikanov & Boeck (2011). The equations of motion are discretized on a structured mesh by an explicit second-order finite-difference scheme with a collocated grid arrangement. The incompressibility constraint is satisfied by a standard projection method. The formulations proposed by Morinishi *et al.* (1998) and Ni *et al.* (2007) are incorporated into the code making the present numerical scheme conservative for mass, momentum and electric charge. We use a hyperbolic-tangent-based stretching to refine the grid in the boundary layers, i.e. the grid is non-uniform in the spanwise y and wall-normal vertical z directions. In particular, the stretching function is given by (Krasnov *et al.* 2011)

$$y = \frac{\tanh(\alpha_y \eta)}{\tanh(\alpha_y)} \tag{2.13}$$

where η is the coordinate on a uniform grid, y denotes the transformed coordinate, while α_y is the stretching coefficient. Equivalent stretching is applied in the z direction. In the streamwise x direction, we use periodic boundary conditions and a uniform grid spacing, and can thus apply fast Fourier transformation (FFT). This allows us to solve the Poisson equations for the pressure and the electric potential with the 2D Poisson solver FishPack (Adams, Swarztrauber & Sweet 1999). Verifications of the code versus a spectral code and more details on the algorithm can be found in Krasnov *et al.* (2011).

The periodic streamwise boundary conditions simplify the solution of the Poisson equation. FishPack is comparatively fast and uses a direct method. The resulting drawback is to ensure that a laminar unperturbed duct flow profile is maintained upstream of the magnetic dipole. Thus, the computational domain has to be increased with increasing Reynolds number when the flow is below the threshold to transition to turbulence. In case of low Reynolds numbers, $Re \lesssim 10$, a periodicity length of 5π was sufficient for the laminar duct profile to be completely reestablished at the end of the domain. For $Re = 100$, a length of 20π was required. This procedure therefore increases the computational cost rapidly when Re is enhanced.

For higher Reynolds numbers, e.g. $Re = 2000$, the flow may become turbulent and this strategy breaks down completely. The conflict with the periodic boundary conditions is circumvented by the application of an additional fringe force which acts

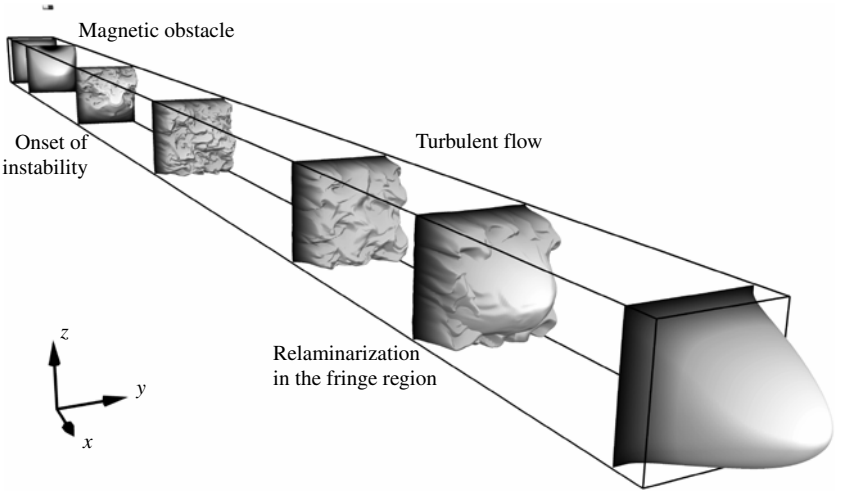

FIGURE 3. Sketch of principle of the fringe force method. The incoming laminar flow is deflected by the dipole which acts as a magnetic obstacle. The flow is strongly deformed and can become turbulent in the wake of the dipole. In the region close to the end of the duct, the fringe force relaminarizes the flow such that the flow profile is laminar again at the end of the computational domain. This method allows the usage of periodic boundary conditions in the streamwise direction.

in the final downstream section of the duct and relaminarizes the transient or turbulent flow (Nordström, Nordin & Henningson 1999). It is sometimes also referred to as the sponge method and is frequently used in studies of turbulent boundary layers (Albrecht *et al.* 2006; Simens *et al.* 2009).

The fringe method is based on an artificial body force $\boldsymbol{F}_{Fringe} = \lambda(\boldsymbol{u}_{laminar} - \boldsymbol{u})$. This fringe force is added to the right-hand side of the Navier–Stokes equation (2.6). It affects the flow only when the prefactor $\lambda(x)$ is non-zero. The shape of the prefactor function is in our cases given by a step function with smoothed edges (Albrecht *et al.* 2006). More precisely, it is given by

$$\lambda(x) = \lambda_{max}\left[S\left(\frac{x - x_{start}}{\Delta_{rise}}\right) - S\left(\frac{x - x_{end}}{\Delta_{fall}} + 1\right)\right] \tag{2.14}$$

with

$$S(\xi) = \begin{cases} 0, & \xi \leqslant 0 \\ 0.5 - 0.5\cos(\xi\pi), & 0 < \xi < 1 \\ 1, & \xi \geqslant 1. \end{cases} \tag{2.15}$$

We studied the influence of the parameters, i.e. the maximal amplitude λ_{max}, steepness of the curve in the beginning Δ_{rise} and in the end Δ_{fall} as well as the total length $|x_{end} - x_{start}|$ of the fringe zone. These tests showed that $\lambda(x)$ has to be smooth and periodic. The particular shape is not important. Typical values in the calculation are $\lambda_{max} = 1$, $\Delta_{rise} = \pi$, $\Delta_{fall} = \pi/2$ and $|x_{end} - x_{start}| = 3\pi$. Preliminary results with this method were already presented in Tympel *et al.* (2012). An example for the resulting velocity profiles is shown in figure 3. Here, the transformation of the flow by the magnetic dipole for $h = 1.6$, $Re = 3000$ and $Ha = 100$ is illustrated. This computation was performed with $4096 \times 192 \times 192$ grid points in x, y and z directions, stretched

		$n_x \times n_y \times n_z$	L_x	$\alpha_{y/z}$	$\min \Delta_{y/z}$	$\max \Delta_{y/z}$	$\lvert F_x \rvert$	$\lvert I_2(0) \rvert$	$\lvert I_4(0) \rvert$
$Re = 10$,	⋆	$1024 \times 96 \times 96$	5π	1.5	0.0064	0.0345	1.1734	0.2390	3.5758
$h = 0.4$		$4096 \times 256 \times 256$	5π	1.5	0.0024	0.0129	1.1497	0.2354	3.5623
$Re = 1000$,		$2048 \times 48 \times 48$	30π	2.0	0.0078	0.0862	0.3050	0.1545	0.1080
$h = 1.6$		$3072 \times 64 \times 64$	30π	2.0	0.0055	0.0647	0.3080	0.1544	0.1089
		$4096 \times 96 \times 96$	30π	2.0	0.0034	0.0432	0.3101	0.1545	0.1096
	⋆	$2048 \times 96 \times 96$	15π	2.0	0.0034	0.0432	0.3102	0.1545	0.1096
		$6144 \times 128 \times 128$	30π	2.0	0.0024	0.0324	0.3111	0.1547	0.1099
		$8192 \times 192 \times 192$	30π	2.0	0.0016	0.0216	0.3120	0.1550	0.1101
$Re = 2000$,		$1024 \times 48 \times 48$	30π	2.0	0.0078	0.0862	0.1612	0.0386	0.0252
$h = 1.6$		$1728 \times 80 \times 80$	30π	2.0	0.0038	0.0518	0.1635	0.0365	0.0255
		$2048 \times 96 \times 96$	30π	2.0	0.0034	0.0432	0.1639	0.0367	0.0256
	⋆	$2048 \times 96 \times 96$	15π	2.0	0.0034	0.0432	0.1639	0.0367	0.0256
		$4096 \times 96 \times 96$	30π	2.0	0.0034	0.0432	0.1639	0.0367	0.0256
		$4096 \times 128 \times 128$	30π	2.0	0.0024	0.0324	0.1645	0.0367	0.0256
		$8192 \times 256 \times 256$	30π	1.5	0.0024	0.0129	0.1650	0.0366	0.0257
		$8192 \times 256 \times 256$	30π	1.75	0.0017	0.0145	0.1650	0.0366	0.0257

TABLE 1. Results of the resolution study for three different parameter sets with spanwise oriented dipole at $Ha = 100$. The symbol ⋆ indicates the resolution that is applied in the parameter studies. Properties of the grids are the number of grid points $n_x \times n_y \times n_z$, streamwise length of computational domain L_x, and the stretching coefficient $\alpha_y = \alpha_z$ in the y and z directions with resulting minimal and maximal grid spacing $\min \Delta_{y/z}$ and $\max \Delta_{y/z}$, respectively. Grid convergence is studied with the streamwise Lorentz force F_x (cf. (3.7)), the change of the streamwise momentum flux I_2 and the wall shear stresses I_4 in a cross-section at $x = 0$ (cf. (3.3) and (3.5)). Values for $Re = 2000$ are time-averaged as in § 4.

with a coefficient of $\alpha_y = \alpha_z = 2$. The streamwise extent of the computational domain is 30π. Owing to high computational costs, it is not possible to perform a detailed parameter study with such fine grids.

We performed a grid sensitivity study for three typical parameter sets which are summarized in table 1. In order to resolve the boundary layers and the steep gradients of the magnetic field close to the point dipole properly, we apply a strong grid clustering in the y and z directions. To elucidate the impact, the corresponding minimal and maximal grid spacing are given. We use three characteristic values to determine whether the resolution is sufficient or not. The first is the total streamwise Lorentz force F_x (cf. equation (3.7)) as it is highly dependent on the velocity and the magnetic field. Second, we compare two integrals over the cross-section at $x = 0$: the change of the streamwise momentum flux I_2 and the wall shear stresses I_4 (cf. equations (3.3) and (3.5)).

The study confirms that the resolution used in our investigations is sufficient to capture the flow dynamics. For instance in case of $Re = 10$, $Ha = 100$, $h = 0.4$ and a spanwise oriented dipole, which represents the basic setting in § 3, the difference between the resulting Lorentz forces of the applied grid with 1024×96^2 and the finest grid with 4096×256^2 points is approximately 2 %. For the transient flow at higher Reynolds numbers and the parameter studies in § 4, we attempt to achieve resolutions similar to Gavrilakis (1992) or Huser & Biringen (1993). This results in a resolution of 2048×96^2 grid points for a streamwise domain length of 15π. In addition, the

total force of this grid is only 0.6 % lower than for the finest grid. Furthermore, the resolution study shows that the same physical effects (e.g. the vortex shedding that is described in § 4) are still obtained with a coarser resolution of 1024×48^2. All values for $Re = 2000$ are time-averaged over 3168 snapshots. To exclude errors due to the time-averaging, the grid sensitivity study was repeated for $Re = 1000$. Again, the total force differs only by 0.7 % for the used grid. In addition, the velocity field itself was compared along a line right below the dipole ($x = 0$ and $z = 0.98$): the maximal error is less than 0.1 % for all velocity components and less than 0.2 % for all components of the Lorentz force density, respectively.

3. Stationary flow at lower Reynolds numbers

3.1. *Mechanisms of flow profile deformation*

In the following, we discuss the behaviour of the flow in case of low Reynolds numbers. As a first step, we take a closer look at the particular deformation of the velocity profile for a Reynolds number $Re = 10$ and a Hartmann number $Ha = 100$. It is observed that differences in the deflection depend on the orientation of the magnetic moment of the dipole.

For low Reynolds numbers, pressure gradient and Lorentz forces balance in the core of the flow provided that the magnetic field is sufficiently strong. This solution is usually not compatible with the conditions at walls. When the magnetic field has a sufficiently strong wall-normal component, the tangential force balance at a wall gives rise to an electromagnetic boundary layer called the Hartmann layer. The velocity difference across this layer is related to an electric current parallel to the wall and perpendicular to the outer velocity (Shercliff 1965). Hartmann layers can be formed whenever their thickness is small compared with the lateral variation of the flow and magnetic field. Their appearance is therefore not restricted to uniform fields.

In the problem at hand, the Hartmann layers are regions where the velocity at the outer edge is controlled by the current in the layer. These currents in the Hartmann layers are generated by the electromotive force $\boldsymbol{u} \times \boldsymbol{B}$ in the core. Since the flow is dominated by the streamwise velocity component, we can infer the current pattern from the distribution of the magnetic dipole field. The Hartmann layers then typically indicate a local acceleration of the flow, which affects the velocity distribution in its vicinity. In the following, we shall focus on the characteristic current distribution for a velocity field dominated by the streamwise component. The associated Lorentz forces and Hartmann layers for this current distribution indicate how the flow field is transformed.

Let us consider the case of a magnetic dipole in the spanwise direction, i.e. $\boldsymbol{m} \parallel \boldsymbol{e}_y$. The magnetic field is perpendicular to the flow direction and parallel to the top wall when the dipole is not too close to the duct. The magnetic field is of high magnitude and strongly inhomogeneous in the cross-section directly below the dipole, i.e. at $x = 0$ (figure 4). The induced current density is the result of the electromotive force $\boldsymbol{u} \times \boldsymbol{B}$ and the induced electric field represented by the gradient of the electric potential. In the bulk, the currents qualitatively conform to the electromotive force $\boldsymbol{u} \times \boldsymbol{B}$. Differences arise near the walls where the currents have to close because of $\boldsymbol{\nabla} \cdot \boldsymbol{j} = 0$. Figure 4(*a*) shows that there are two stagnation points in the streamline pattern of the electric currents based on the laminar velocity distribution. They are close to the surface. Figure 4(*b*) shows that the essential properties of the current distribution are preserved for the modified flow field. The streamlines have been obtained from a numerical simulation and are projected into the cross-section. What

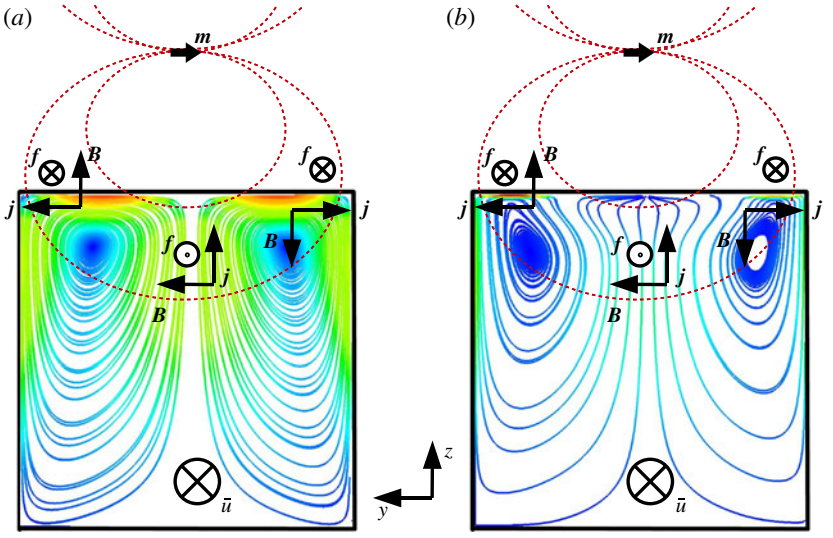

FIGURE 4. (Colour online) Sketch of principle for the acting forces in the case of spanwise-oriented magnetic dipole for (*a*) a laminar base flow and (*b*) the deflected flow. Streamlines (solid) represent the electric currents in the cross-section with $x = 0$ for Reynolds number $Re = 2000$, Hartmann number $Ha = 100$ and dipole distance of $h = 1.6$. The dashed lines (shown in red online) indicate the magnetic field lines. Arrows denote the local main direction of the magnetic field and the currents. In the Hartmann layers (top corners of the duct), the resulting Lorentz force points then in the same direction as the mean velocity. In the centreline, the Lorentz force brakes the fluid and, if strong enough, drives the vortex formation.

may look like a sink or a source in figure 4(*b*) can be explained as a result of the projection on the two-dimensional cross-section.

With the obtained current density, one may now estimate the resulting Lorentz force distribution $\boldsymbol{f} \sim \boldsymbol{j} \times \boldsymbol{B}$ in the duct which will result in a braking force in the bulk of the flow. It should be emphasized that this braking force is also present in the region directly below the dipole. Here, the magnetic field has the largest magnitude. If this force is strong enough, which is the case when the Hartmann number is sufficiently large, a local flow reversal is observed. The resulting vortices in figures 5(*a*) and 6(*a*) mark now the areas with strong spanwise magnetic field. In the top corners, the situation is different. As the current density field lines close here, the resulting Lorentz force accelerates the flow. Thus, local Hartmann layers are created. These layers are of interest when the influence of the Hartmann number is investigated in § 4.3. In contrast to the classical Hartmann flow configuration (Hartmann 1937; Hartmann & Lazarus 1937), the local Hartmann layer is present at the top wall and practically absent at the bottom wall. As a consequence, the flow distortion decreases rapidly when moving from the top to the bottom wall. This is illustrated in figure 6 by a second set of streamlines seeded at a distance of 0.05 length units above the bottom wall. Nonetheless, local Hartmann layers also appear for the other dipole orientations where the normal component of the magnetic field is sufficiently strong at a wall. In the case of a streamwise dipole orientation, strong Hartmann layers are found at the centreline ahead and behind the dipole position. Much less pronounced layers are also found at the sides.

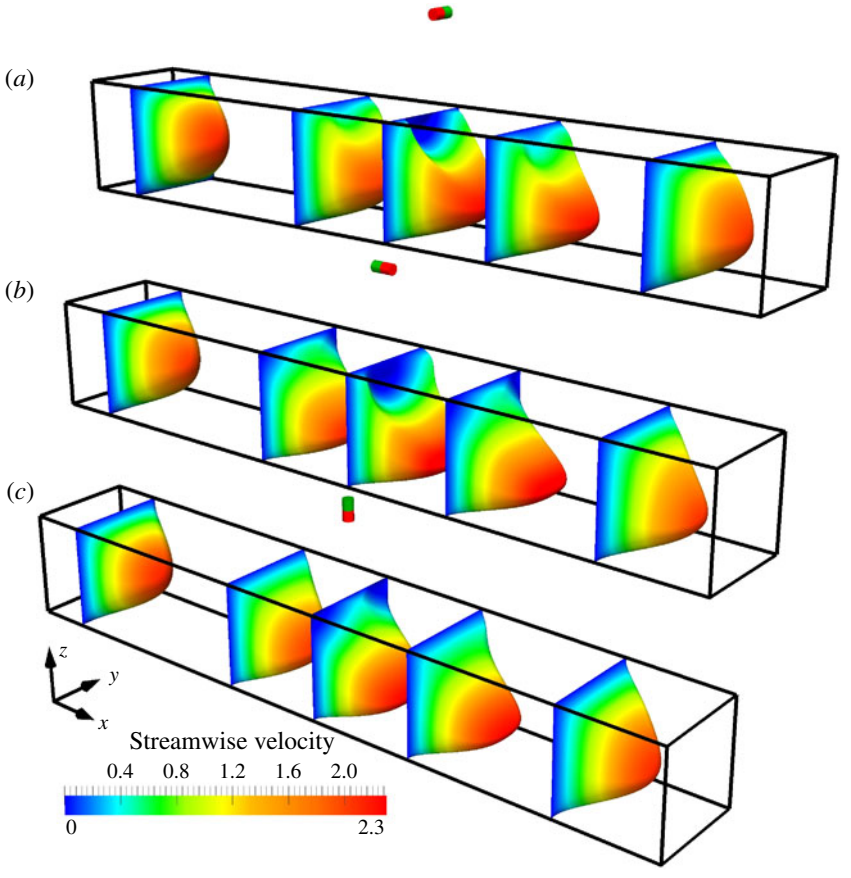

FIGURE 5. The point dipole as a magnetic obstacle: contours of the streamwise velocity at various positions along the duct illustrate the effect of a point dipole on the duct flow dynamics. From left to right: $x = -3, -1, 0, 1, 2.5$. The total duct length is 5π and $Re = 10$, $Ha = 100$ and $h = 1.6$. Three different orientations of the dipole are presented: (*a*) spanwise, (*b*) streamwise and (*c*) vertical magnetic moment.

For the same reasons, one observes a well-pronounced local Hartmann layer positioned directly below a vertical dipole, i.e. $\boldsymbol{m} \parallel \boldsymbol{e}_z$. Here, the main component of the magnetic field is in vertical direction and thus perpendicular to the flow direction and to the top wall. These layers can be observed in figures 5(*c*) and 6(*c*). In addition, two vortices are created in the top corners. One may understand the case of the vertical dipole as counterpart of the spanwise case as it forms Hartmann layers where the other shows areas of reversed flow and vice versa. Moreover, the vertical dipole induces spanwise-oriented currents in the bulk as it is the case for a homogeneous vertical field. Consequently, the total Lorentz force appears again as a braking force.

In the case of streamwise magnetic moment, i.e. $\boldsymbol{m} \parallel \boldsymbol{e}_x$, one observes five well-pronounced vortices at the top as shown in figure 6(*b*). The four small vortices in figure 6(*b*) are located upstream and downstream of the dipole at positions where local Hartmann layers appear along the centreline. In this region, the currents in the bulk are in the spanwise direction. They close near the upper and lower walls. This is the reason for a braking Lorentz force near the lateral walls caused by the

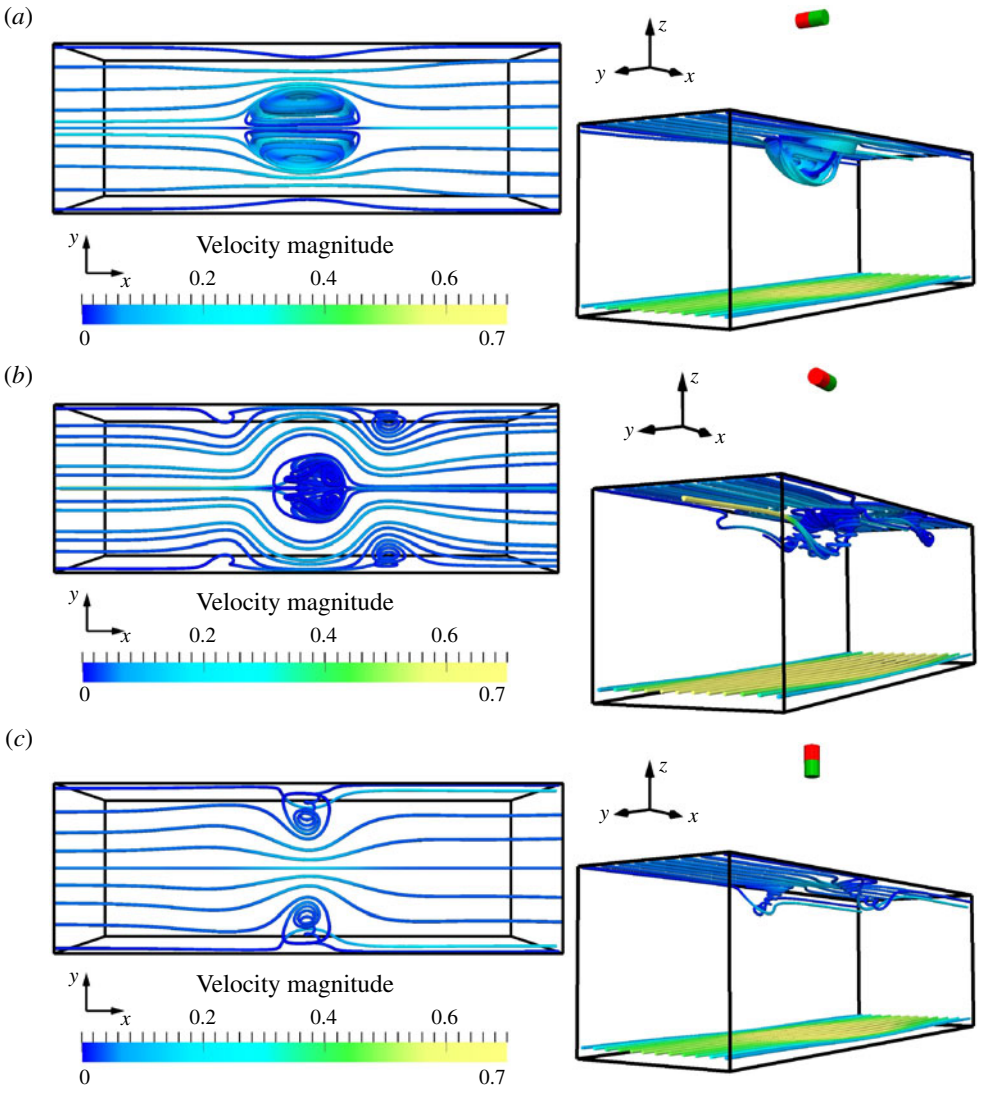

FIGURE 6. (Colour online) Velocity field streamlines for different orientations of the dipole at $Re = 10$, $Ha = 100$ and $h = 1.6$. Dipole orientations are (*a*) spanwise, (*b*) streamwise and (*c*) vertical. The local Hartmann layer is visible due to higher velocities at the top surface. Vortices and flow structures are always three-dimensional. All three configurations are shown from two different perspectives in each case: left is a top view and right a side view. The box indicates the duct from $x = -3$ to $x = 3$. The total length of the duct was 5π.

spanwise component of the magnetic field. At the centreline, the flow is accelerated in the Hartmann layer. This Lorentz force distribution causes regions of reversed and accelerated flow. The strongly pronounced vortex directly below the dipole is not directly generated by the magnetic field. The main component of the magnetic field in this area is the streamwise component and thus parallel to the mean flow direction and the top wall. A streamwise magnetic field cannot produce an electric current and therefore the action of the Lorentz force vanishes right below the streamwise-

oriented dipole. Nevertheless, vortices such as just discussed have been observed for the streamwise-oriented dipole at several Reynolds numbers and strong Hartmann numbers. The origin of this vortex may be found in the local Hartmann layers that surround the vortex. The Lorentz forces affect the liquid at the top as follows. The flow is first accelerated at the centreline, then pushed aside to the two Hartmann layers close to the edges and finally again accelerated at the centreline. This forcing leaves the liquid right below the dipole no other possibility, but to swirl and to form a vortex. One has to mention here that this explanation is more or less descriptive and that the flow is always fully three-dimensional as indicated in figure 6(*b*).

An alternative explanation of the flow modification might be given by means of the characteristic surfaces in creeping MHD flows, which have been introduced by Kulikovskii (1968). These surfaces can be defined when pressure gradient and Lorentz force balance in the core of the flow. They are spanned by the parts of the magnetic field lines within the flow that have a constant value of the line integral $\int \mathrm{d}s/\|\boldsymbol{B}\|$. Under certain additional assumptions, the flow will be parallel to these surfaces (Alboussiére, Garandet & Moreau 1996; Alboussiére 2001). One may therefore expect the flow to avoid the regions enclosed by field lines with a certain magnitude of the magnetic field. For the streamwise and spanwise orientations this would be a roughly hemispherical region directly beneath the dipole. For the vertical dipole orientation, there would be two such domains to the left and to the right of the dipole. This is also in qualitative agreement with the specific arguments based on the current distribution that we have discussed before.

So far, we have reported the velocity profiles and the streamlines of the flow. These plots give us information on the flow structures, but not on the Lorentz force components in the flow. In order to proceed, we quantify the influence of the dipole on the flow with an integral criterion for the balance of Lorentz force, pressure gradient and wall stresses. Such a balance equation is obtained directly from the Navier–Stokes equation (2.6). We integrate the x component of (2.6) with respect to y and z and apply the assumptions that the velocity field is smooth and stationary and that the volume flux is constant and normalized to 1. The balance equation is

$$I_1 + I_2 - I_3 + I_4 = 0. \tag{3.1}$$

It contains the Lorentz force term

$$I_1 = \iint_{[-1,1]^2} f_x \,\mathrm{d}y\,\mathrm{d}z, \tag{3.2}$$

the change of the streamwise momentum flux

$$I_2 = -\iint_{[-1,1]^2} \partial_x(u_x^2)\,\mathrm{d}y\,\mathrm{d}z, \tag{3.3}$$

the friction coefficient

$$I_3 = \iint_{[-1,1]^2} \partial_x p\,\mathrm{d}y\,\mathrm{d}z \tag{3.4}$$

and the contribution of the wall shear stresses

$$I_4 = \frac{1}{Re}\left(\int_{-1}^{1} \left[\partial_y u_x\right]_{y=\pm1}\mathrm{d}z + \int_{-1}^{1} \left[\partial_z u_x\right]_{z=\pm1}\mathrm{d}y\right). \tag{3.5}$$

For a homogeneous magnetic field, the integral of the Lorentz force per cross-section vanishes. In the case of a laminar flow, wall stresses are balanced by the pressure

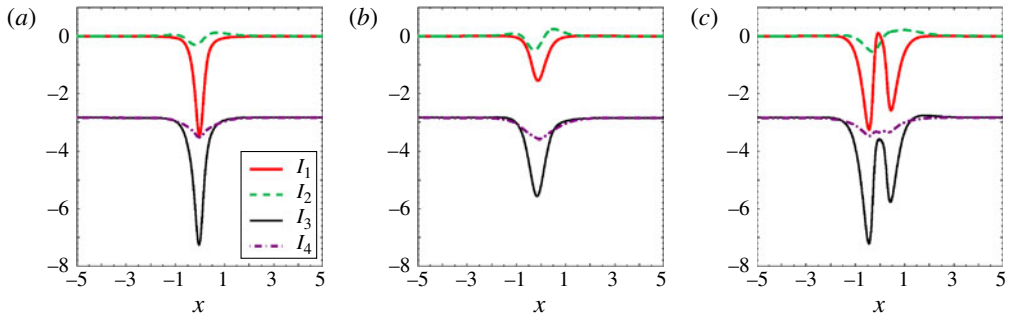

FIGURE 7. (Colour online) Terms of the integrated momentum balance as given by (3.2)–(3.5) at $Re = 10$, $Ha = 100$ and $h = 0.4$. Streamwise profiles for different dipole orientations are shown: (*a*) vertical, (*b*) spanwise and (*c*) streamwise.

gradient. With an inhomogeneous magnetic field present, the question of which hydrodynamic forces balance the appearing Lorentz forces arises. Figure 7 shows all terms of the balance equation (3.1) for the three dipole orientations.

We can see that the contribution to the Lorentz force is mainly based on the presence of the local Hartmann layers. Therefore, the forces are much stronger for the vertical case than for the spanwise case. The strongest contribution of the Lorentz force comes from the streamwise-oriented dipole. Here, two Hartmann layers are clearly visible, ahead and behind the dipole positioned at $x = 0$. It also becomes clear that it is mainly the pressure gradient which balances the Lorentz force. The nonlinear term I_2 is small due to the low Reynolds number of $Re = 10$. In § 4, we will come back to this point and will see that the nonlinear term has a stronger influence as expected for higher Reynolds numbers. Before increasing the Reynolds number, we study the influence of the Hartmann number at fixed $Re = 10$.

3.2. *Hartmann number dependence at fixed Reynolds number*

The following scalar integral measure

$$\mathscr{A}(x) = \frac{\iint |\boldsymbol{u} - \boldsymbol{u}_{lam}| \,\mathrm{d}y\,\mathrm{d}z}{\iint |\boldsymbol{u}_{lam}| \,\mathrm{d}y\,\mathrm{d}z} \tag{3.6}$$

will be used for quantification of the distortion of the laminar profile $\boldsymbol{u}_{lam}$ caused by the magnetic obstacle. An example for the distortion is shown in figure 8 for a Reynolds number of 10 and a wall-normal-oriented dipole in a distance $h = 0.4$. The graphs compare the distortion for several Hartmann numbers which are indicated in the legend. Two effects are observed. First, there is almost no distortion of the flow for $Ha < 25$. In this range, the resulting forces behave to a good approximation as in the kinematic case for an unperturbed flow. They are also comparable with the experiments by Heinicke *et al.* (2012) in this parameter range. Second, the maximal amplitude of $\mathscr{A}$ increases approximately linearly with the Hartmann number for $Ha > 25$. Nevertheless, one can assume a saturation of this deformation for very high Hartmann numbers due to the finite duct geometry. Furthermore, the starting point of the deflection is shifted upstream with increasing Hartmann number. In particular, it changes from $x \approx -1$ for $Ha = 25$ to $x \approx -3$ for $Ha = 200$. In all cases the distortion

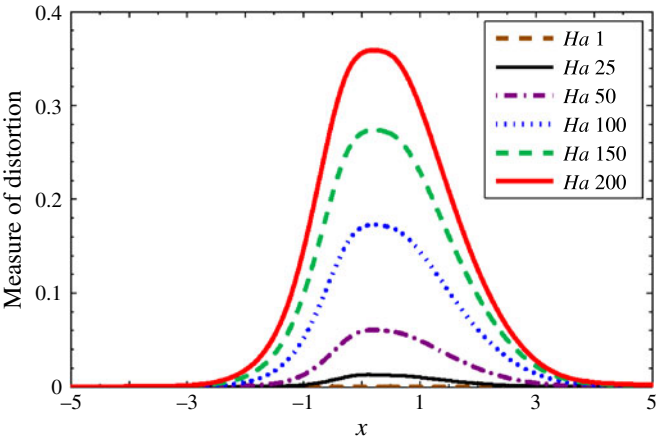

FIGURE 8. (Colour online) Distortion of the laminar duct flow as a function of the Hartmann number for a low Reynolds number duct flow at $Re = 10$. Deflection of the flow in dependence of Hartmann number as quantified by $\mathscr{A}$.

subsides at approximately four characteristic lengths downstream of the dipole position. Therefore, the curves become slightly more symmetric for higher Hartmann numbers.

Let us now focus on the integral forces and torques. Therefore, we define the total Lorentz force by

$$\boldsymbol{F} = \int_V \boldsymbol{f}\,\mathrm{d}V = \int_V \frac{Ha^2}{Re}(-\nabla\phi + \boldsymbol{u}\times\boldsymbol{B})\times\boldsymbol{B}\,\mathrm{d}V, \tag{3.7}$$

and the total torque as

$$\boldsymbol{T} = \int_V \boldsymbol{r}\times\boldsymbol{f}\,\mathrm{d}V \tag{3.8}$$

with $\boldsymbol{r} = \boldsymbol{x} - (h+1)\boldsymbol{e}_z$. Calculations are done for the three main dipole orientations. The dependence of the integral forces on Reynolds and Hartmann number was found to be practically the same for all orientations. More interestingly, the absolute values of the forces were found to differ at the same values of Hartmann and Reynolds numbers. The streamwise-oriented dipole gave always stronger forces than the wall-normal vertical dipole. It has to be recalled that the Hartmann number is based on B_{max}, the maximal value of the magnetic field inside the duct, and not on the magnetic moment of the dipole. Thus, in an experiment using a real magnet, it is always found that a rotation of the magnetic dipole from vertical to streamwise orientation will cause a decrease of the forces simply because such a rotation will decrease the Hartmann number by a factor of two in correspondence with equation (2.2). In all cases, the spanwise-oriented dipole will give the weakest force. The integral torque component behaves in the same way as the forces. The torque is zero for the spanwise dipole orientation due to the symmetry of the problem.

In figure 9, we compare the total drag force, i.e. the streamwise force component, the total lift force, i.e. the vertical force component (*a,b*), and the total torque (*c,d*) for the wall-normal and streamwise orientation of the dipole. We observe that the drag force is higher than the lift force. The data in figure 9 reveal three power laws which seem to be valid up to $Ha \approx 25$. For higher Hartmann number values the growth with

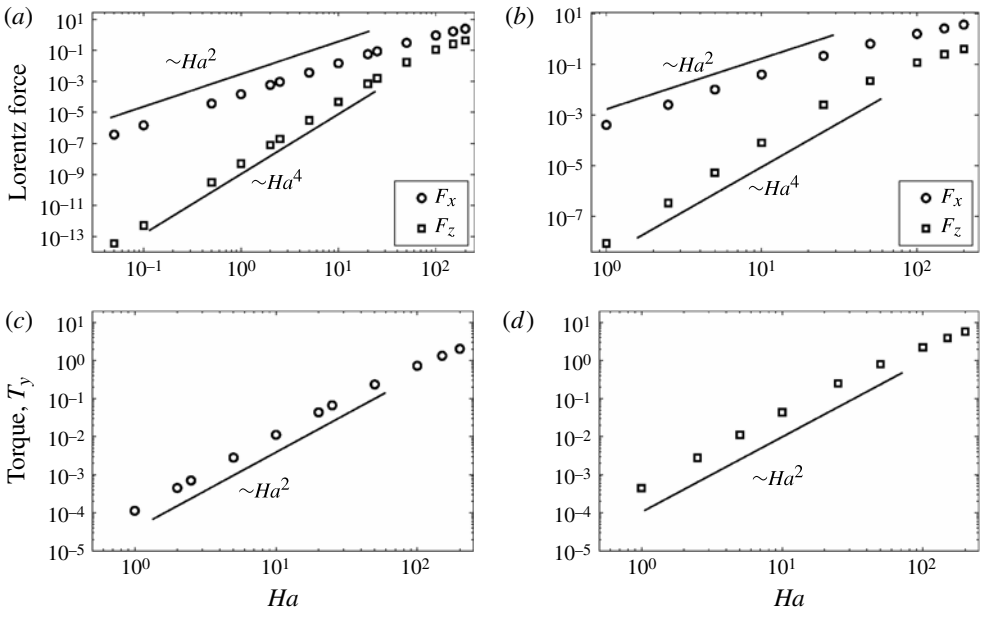

FIGURE 9. Drag and lift forces and resulting torque as a function of the Hartmann number for $Re = 10$ and $h = 0.4$. (*a,c*) Wall-normal orientation of the dipole. (*b,d*) Streamwise orientation of the dipole.

Ha becomes weaker. As expected, one finds that the drag force $F_x \sim Ha^2$ and that the torque component $T_y \sim Ha^2$. These power laws are caused by the fact that Ha^2/Re is a prefactor to the Lorentz force term in the momentum balance. The third power law for the lift force is found as $F_z \sim Ha^4$. This behaviour of the lift force is not immediately obvious. We explain it by the following argument.

Let $\boldsymbol{u}$ be a solution to the Navier–Stokes equation (2.6) for a given Hartmann and Reynolds number. Similar to a perturbation expansion in weakly nonlinear flows, we divide the velocity field into three parts,

$$\boldsymbol{u} = \boldsymbol{u}_0 + \boldsymbol{u}_1 + \boldsymbol{u}_2. \tag{3.9}$$

Here, $\boldsymbol{u}_0$ is the base flow, $\boldsymbol{u}_1$ describes the distortion of the base flow and $\boldsymbol{u}_2$ stands for a higher-order nonlinear term. The base flow $\boldsymbol{u}_0$ is the flow in the limit of small interaction parameter Ha^2/Re and low Reynolds number. It is supposed to be a steady flow which is solely driven by the pressure gradient. Thus, $\boldsymbol{u}_0$ is the solution of

$$0 = -\nabla p + \frac{1}{Re}\nabla^2 \boldsymbol{u}_0. \tag{3.10}$$

This solution is the laminar flow $\boldsymbol{u}_{lam}$ which can be derived analytically (Pozrikidis 1997). As was shown by Heinicke *et al.* (2012), the Lorentz forces for a given laminar profile and for the full Navier–Stokes equation (2.6) are almost the same in the case of Hartmann and Reynolds numbers below certain thresholds. The present case of $Ha = 25$ and $Re = 10$ satisfies these thresholds and the approximation with a laminar profile $\boldsymbol{u}_{lam}$ gives a good agreement for the drag component of the Lorentz force. However, the lift force is zero for a laminar velocity profile.

The second term $\boldsymbol{u}_1$ describes the deflection due to the dipole. It is again an approximation which holds for small Reynolds numbers. Again, this flow is steady. Viscous forces are balanced by the Lorentz force

$$\frac{1}{Re}\nabla^2\boldsymbol{u}_1 \approx -\frac{Ha^2}{Re}(-\nabla\phi_0 + \boldsymbol{u}_0 \times \boldsymbol{B}) \times \boldsymbol{B}. \tag{3.11}$$

It is clear from this equation that the amplitude $u_1 \sim Ha^2$. We note that an additional pressure correction is necessary to maintain incompressibility. The contribution $\boldsymbol{u}_1$ does not give a contribution to the lift force. This can be shown with the following argumentation based on Stokes flow. Assume that there is a non-zero lift force F_z. On the one hand, the linearity of the equations implies that a sign reversal of pressure and $\boldsymbol{u}_0 + \boldsymbol{u}_1$, respectively, results in an opposite force. In particular, the lift force would reverse, i.e. one would obtain $-F_z$. On the other hand, the problem has mirror symmetry with respect to the (y, z) plane containing the dipole, i.e. a reversal of flow direction should change the sign of the drag force F_x but not the sign of the lift force. For this reason $F_z = -F_z$, i.e. the lift force has to vanish.

The third part of the decomposition, $\boldsymbol{u}_2$, is the nonlinear part which mainly reflects effects of inertia. This term is an approximation, but presents the realistic flow pattern for moderate Reynolds numbers. Rewriting (3.9) as $\boldsymbol{u}_2 = \boldsymbol{u} - \boldsymbol{u}_0 - \boldsymbol{u}_1$ in the Navier–Stokes equation (2.6) for the steady flow case and neglecting all terms of order $O(Ha^4)$ leads to

$$\nabla^2\boldsymbol{u}_2 = Re\,((\boldsymbol{u}_1 \cdot \nabla)\boldsymbol{u}_0 + (\boldsymbol{u}_0 \cdot \nabla)\boldsymbol{u}_1)\,. \tag{3.12}$$

From this equation, one can estimate that $u_2/\ell^2 \approx Re\,u_1u_0/\ell \approx Re\,Ha^2\,u_0^2\ell$. Thus, $u_2 \approx Re\,Ha^2\,u_0^2\ell^3$ which gives rise to the lift force $F_z \approx (Ha^2/Re)u_2$ and thus the expected Hartmann number dependence of Ha^4 for the lift force. In this estimate we used ℓ to denote the non-dimensional characteristic gradient variation scale given in units of the duct half-width. It was also numerically verified that the lift force vanishes when the nonlinear term $(\boldsymbol{u} \cdot \nabla)\boldsymbol{u}$ is artificially set to zero. In this case, the flow was symmetric in streamwise direction. Thus, the numerical test confirms that the nonlinear term is responsible for non-symmetric pattern in the flow and for the lift force. We also note that a more formal argument could be given using a double expansion in the two small parameters Ha and Re.

3.3. *Reynolds number dependence at fixed Hartmann number*

In addition to the Hartmann number, the second control parameter, Re, will affect the structures of the flow. Following directly from the definition of the Lorentz force, we verify the dependencies $F_x \sim 1/Re$ and $T_y \sim 1/Re$, respectively, which are shown in figure 10 for several Hartmann numbers. Furthermore, we see that the lift force F_z is constant at a given Hartmann number for $Re < 1$ as already discussed above. In case of higher Reynolds number, the lift force data decay steeper than $1/Re$.

With increasing Reynolds number the contributions of the nonlinear advection term will increase and manifest in an increasing distortion of the flow. We observe that the distortion in the wake, as measured by (3.6), decays almost exponentially, i.e. as a function $\exp(-\alpha x)$ with respect to the streamwise direction obeying a spatial decay rate α. This is demonstrated in figure 11 for a Hartmann number of $Ha = 100$ in a logarithmic–linear plot. The first observation is that the maximum of the distortion is decreasing with increasing Reynolds number: an effect of the decaying interaction parameter Ha^2/Re. The decay of the maximal value may also be considered as an

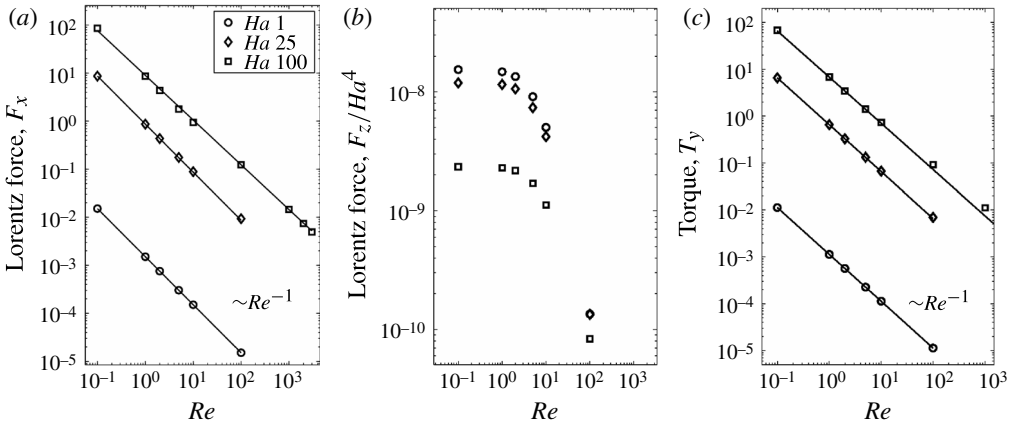

FIGURE 10. Reynolds number dependence of the force components and the torque: (*a*) drag force F_x; (*b*) lift force F_z compensated by Ha^4; (*c*) torque T_y. Data are for a wall-normal magnetic point dipole at a distance of $h = 0.4$. The dependence $1/Re$ is indicated by a solid line for the drag component of the Lorentz force and the torque. Data are obtained for several Hartmann numbers as indicated in the legend.

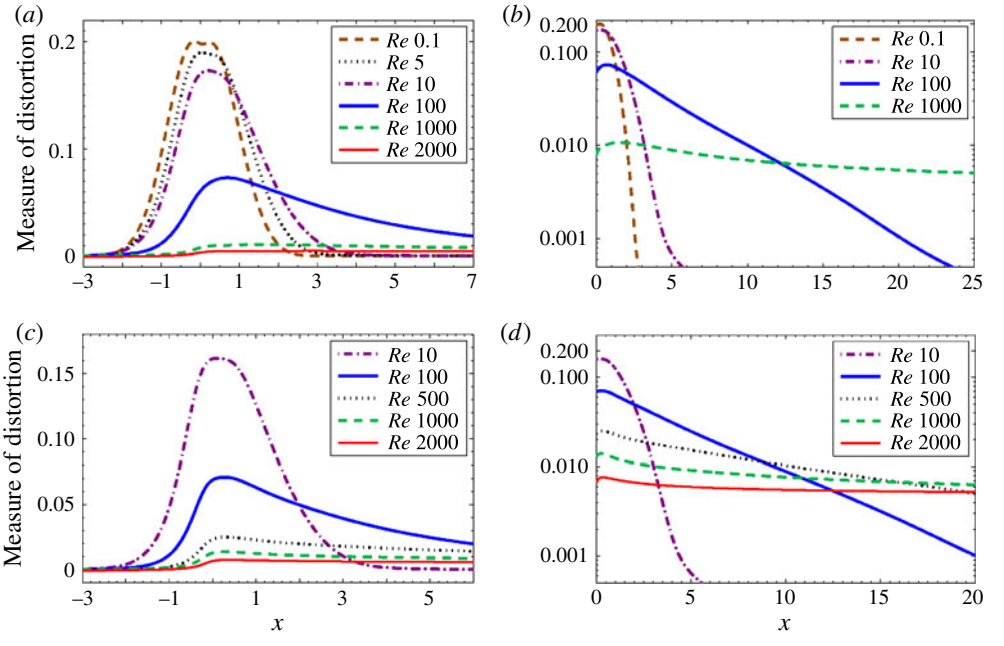

FIGURE 11. (Colour online) Flow distortion as quantified by (3.6) for several Reynolds numbers. In all cases, $Ha = 100$ and $h = 0.4$. The dipole is located at $x = 0$ with (*a*) wall-normal magnetic moment and (*c*) spanwise magnetic moment, respectively. In (*b,d*) we replot the same data on logarithmic–linear axes.

effect of the nonlinear term. A numerical test case shows that the value does not decrease if the nonlinear term is artificially switched off. When the data are presented

in a logarithmic scale, as in figure 11(*d*), the exponential decay is clearly visible. The fit of these data with an exponential function results in a spatial decay rate which is approximately inversely proportional to the Reynolds number.

The Reynolds number dependence of the decay rate can be rationalized from the following consideration for steady flow. The Lorentz force term $(Ha^2/Re)(\boldsymbol{j} \times \boldsymbol{B})$ is a localized force term and will not affect the decay in the wake sufficiently far downstream from the dipole position, i.e. we can drop it in the wake. The Navier–Stokes equations simplify to

$$(\boldsymbol{u} \cdot \boldsymbol{\nabla})\boldsymbol{u} = \frac{1}{Re}\Delta \boldsymbol{u} - \boldsymbol{\nabla} p. \tag{3.13}$$

We now represent the distortion as $\boldsymbol{v} = \boldsymbol{u} - \boldsymbol{u}_{lam}$. If we use this representation, then the dominant term on the left-hand side becomes $u_{lam}\partial_x \boldsymbol{v}$. On subtracting the equation for the laminar flow itself we obtain

$$u_{lam}\partial_x \boldsymbol{v} = \frac{1}{Re}\Delta \boldsymbol{v} - \boldsymbol{\nabla} p', \tag{3.14}$$

where the pressure contribution p' serves to maintain incompressibility. If we further approximate the laminar velocity distribution by its mean value $\bar{u}$ we eventually have

$$\bar{u}\partial_x \boldsymbol{v} = \frac{1}{Re}\Delta \boldsymbol{v} - \boldsymbol{\nabla} p'. \tag{3.15}$$

Following the usual boundary-layer approximation ideas based on $Re \gg 1$ one can further neglect the second derivative with respect to x in the Laplacian. The problem then effectively reduces to a diffusion problem

$$\partial_t \boldsymbol{v} = \frac{1}{Re}\left(\frac{\partial^2}{\partial y^2} + \frac{\partial^2}{\partial z^2}\right)\boldsymbol{v} \tag{3.16}$$

where we have introduced $t = x/\bar{u}$. Using separation of variables, it is clear that the decay of $|\boldsymbol{v}|$ with t is ultimately determined by the largest eigenvalue $-\alpha_1$ of the two-dimensional Laplacian, i.e.

$$|\boldsymbol{v}| \sim \exp(-\alpha_1 t/Re) = \exp(-\alpha_1 x/Re\bar{u}). \tag{3.17}$$

Therefore, the measure of distortion has to decay approximately exponentially. The last steps of our argumentation are more heuristic because we neglect the remaining pressure term. A justification of this step might be not straightforward, but we suppose that it is justified because it amounts to a projection on the space of solenoidal functions, which should not interfere with the gist of the argument. We further note that the spatial decay is independent of the orientation of the magnetic dipole. The numerical simulations show that this is approximately the case for $Ha = 100$ and Re reaching from 10 up to 2000. We also remark that the decay is clearly visible only at large distances from the dipole position. For $Re \gtrsim 500$, it is difficult to identify a clear exponential decay of $\mathscr{A}(x)$ (cf. equation (3.6)) within the computational domain because of the slower decay of higher modes.

To summarize the results for the lower Reynolds numbers: we explained why different transformations of the flow are observed for different dipole orientations leading to the formation of local Hartmann layers and areas of reversed flow due to strong Lorentz forces. The strength of the forces and their effect on the deflection of the flow in dependence on the Hartmann number was also analysed. The total drag force is found to be proportional to Ha^2 and the total lift force is proportional to Ha^4

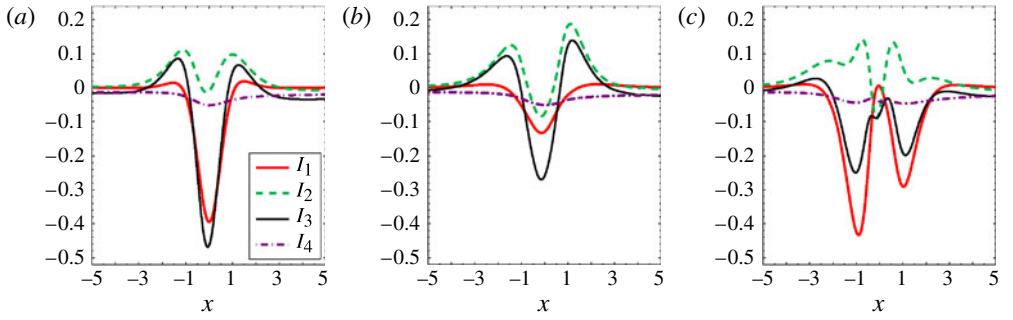

FIGURE 12. (Colour online) Streamwise variation of the different terms of the momentum balance (3.1) averaged over the cross-section at $Re = 2000$, $Ha = 100$ and $h = 1.6$ for three different orientations of the dipole: (*a*) wall-normal vertical, (*b*) spanwise and (*c*) streamwise. Equations (3.2)–(3.5) have been used again. Since the spanwise case in the mid panel is time-dependent, data are time-averaged over one oscillation time of 3.168 time units.

in the present Reynolds number regime. When the Reynolds number is increased, we observe that the length of the wake is increased. It was also shown why the spatial downstream decay of the deflected flow in the wake is proportional to $1/Re$. In the next section, we will see how the vortex formation process changes when the dipole triggers a transition to turbulence as the Reynolds number is increased.

4. Time-dependent flow at higher Reynolds numbers

In this section, we study time-dependent flow structures which start to appear at Reynolds numbers of ∼2000 and higher and for Hartmann numbers above 80. We will observe vortex shedding for cases when the dipole is positioned sufficiently far in a distance of $h = 1.6$ from the top surface of the liquid. For smaller distances than $h = 1.0$ the flow is always stationary in the range of Reynolds numbers which could be covered here ($Re \leqslant 3000$). Therefore, we will restrict our study in this section to the case with $h = 1.6$ which generates qualitatively new features compared to the last section.

4.1. *Deformation of the flow*

The analysis of the different contributions to the momentum balance (3.1) is shown in figure 12 for $Re = 2000$ and $Ha = 100$ for the three dipole orientations: streamwise, spanwise and wall-normal vertical. The deformations of the flow field show effects which are similar to the low-Reynolds-number case from § 3. Since the Reynolds number is higher, the nonlinear term has a stronger influence on the deflection of the flow as visible by its larger magnitude in the figures. The terms of the momentum balance (3.1) reveal that the Lorentz force obeys a qualitatively similar behaviour as in the low Reynolds number cases (cf. also figure 7). It is again the pressure gradient that balances the additional contribution that is now produced by the change of streamwise momentum flux I_2.

The velocity field streamlines for the three cases are shown in figure 13. We observe again the formation of local Hartmann layers and vortices as described for the low Reynolds number runs in § 3. In the case of the spanwise-oriented dipole, a strong vortex in the centre of the duct is formed which becomes now time-dependent, i.e. a vortex shedding is initiated. For streamwise- and wall-normal-oriented dipoles the flow

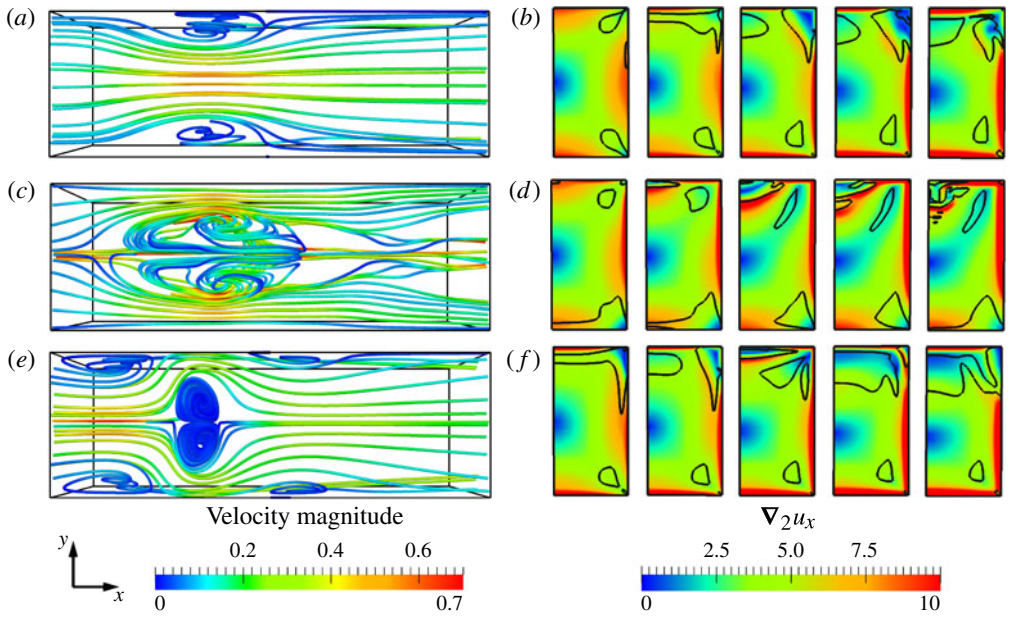

FIGURE 13. Streamlines (*a,c,e*) and inflection lines (*b,d,f*) at $Re = 2000$, $Ha = 100$ and $h = 1.6$ for different orientations. (*a,b*) Wall-normal vertical dipole. (*c,d*) Spanwise-oriented dipole. (*e,f*) Streamwise-oriented dipole. Streamlines are shown along top wall from $x = -2$ until $x = 5$. Colour indicates the velocity magnitude. The panels to the right show the corresponding cross-sections at streamwise positions $x = -2, -1, 0, 1$ and 2. Owing to symmetry only a half-plane is displayed. The background colours display the magnitude of the cross-stream gradient $\boldsymbol{\nabla}_2 u_x$. Black solid lines are the inflection lines as defined in (4.2).

in the wake remains stationary due to the local Hartmann layers that stabilize the flow in the range of Reynolds numbers accessible here.

Stability investigations for the onset of time-dependent flow become less straightforward as the base flow depends on the Hartmann number. Thus, a simplified criterion for two-dimensional flow is applied here. A possible explanation for the instability and transition to a time-dependent flow is shown in figure 13. In the right column of the figure, we show five cross-sections that contain the magnitude of the cross-stream gradient of the streamwise velocity which is determined by $\boldsymbol{\nabla}_2 u_x$ where $\boldsymbol{\nabla}_2$ denotes the gradient with respect to the y and z directions. Furthermore, the inflection point criterion (Uhlmann & Nagata 2006) follows with the definition

$$\boldsymbol{n} = \frac{\boldsymbol{\nabla}_2 u_x}{|\boldsymbol{\nabla}_2 u_x|} \tag{4.1}$$

to

$$\nabla_{\boldsymbol{n}}^2 u_x = 0. \tag{4.2}$$

Criterion (4.2) generalizes the inflection points in one-dimensional velocity profiles. It has been used frequently in order to determine whether a flow can become unstable or not. Contour lines which satisfy (4.2) are added to each of the five cross-section plots in figure 13. We observe that in the case of a spanwise-oriented dipole the magnitude of the gradient close to the inflection line is higher compared with the other cases. Thus, the probability of instability increases. As a consequence, we will restrict our

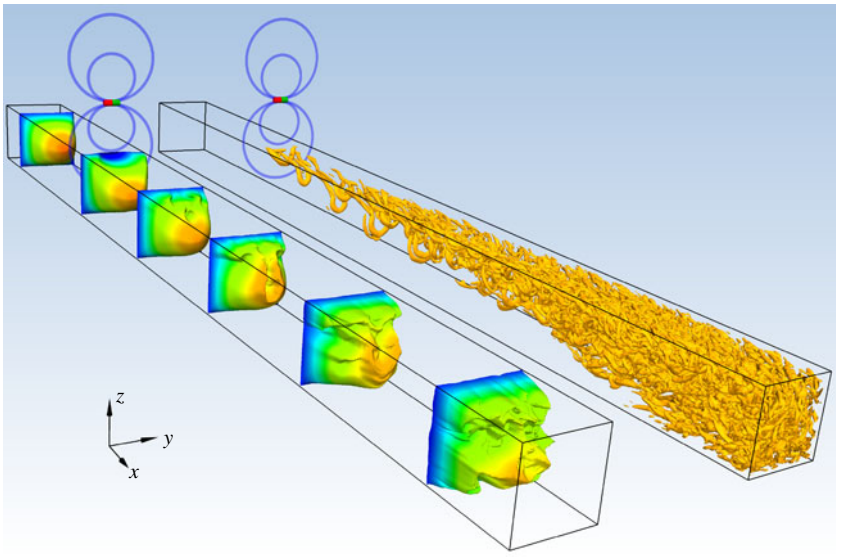

FIGURE 14. Vortex shedding for a spanwise-oriented dipole. Both ducts show the same snapshot for a Reynolds number $Re = 2000$, a Hartmann number $Ha = 100$ and a distance $h = 1.6$. The left duct displays instantaneous velocity profiles taken at 6 different streamwise locations between $x = -10$ and 40. The right figure shows the isocontours of $\lambda_2 = -1$.

observations and parameter studies in this section to the spanwise-oriented dipole, the most interesting case for transition to turbulence. In the subsequent paragraph, we will be concerned with the time-dependent behaviour of the generated vortex structures, i.e. the vortex shedding, and the resulting structures in the wake.

The vortex shedding generates a turbulent wake which is displayed in figure 14. In parallel to several cross-sections of the streamwise velocity along the duct, isocontours of $\lambda_2 = -1$ are shown where λ_2 is the second largest eigenvalue ($\lambda_1 \geqslant \lambda_2 \geqslant \lambda_3$) of the symmetric matrix

$$\Lambda_{ij} = S_{ik}S_{kj} + \Omega_{ik}\Omega_{kj} \tag{4.3}$$

which is composed of the rate of strain and vorticity tensors, respectively,

$$S_{ij} = \frac{1}{2}\left(\frac{\partial u_i}{\partial x_j} + \frac{\partial u_j}{\partial x_i}\right) \quad \text{and} \quad \Omega_{ij} = \frac{1}{2}\left(\frac{\partial u_i}{\partial x_j} - \frac{\partial u_j}{\partial x_i}\right). \tag{4.4}$$

Negative values, $\lambda_2 < 0$, denote vortex cores (Jeong & Hussain 1995) which can be clearly identified as so-called hairpin structures in the figure. They are found close to the top wall in the beginning of the wake before the whole duct is filled with turbulent flow patterns further downstream.

Alternatively, the vortex shedding can be observed by the time signal of the Lorentz force itself. Both the drag force component F_x and the lift force component F_z show a periodic sinusoidal time dependence. The temporal modulation of the signal is weak compared with the absolute magnitude (cf. figure 18 below). For example, it is $F_x = -1.64 \times 10^{-1} \pm 4.67 \times 10^{-4}$ and $F_z = 1.74 \times 10^{-2} \pm 6.75 \times 10^{-4}$ for $Re = 2000$ and $Ha = 100$. Both forces oscillate with a frequency of 3.15×10^{-1} inverse time units.

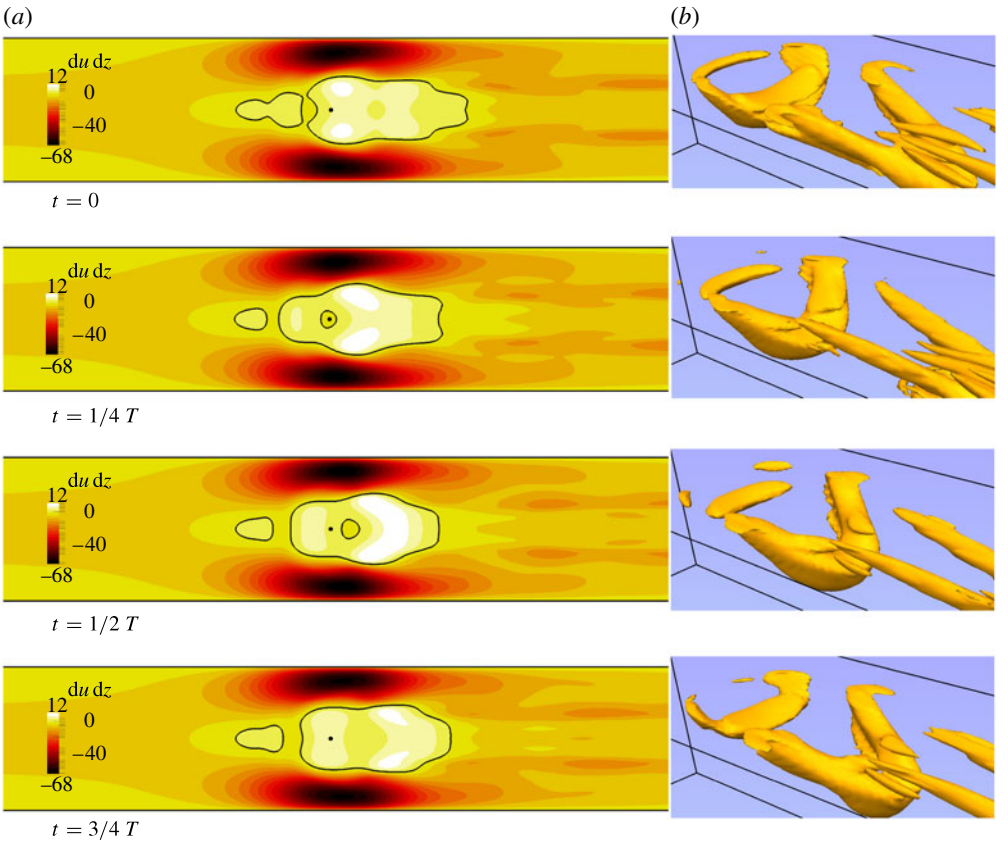

FIGURE 15. (Colour online) Visualization of the time-dependent structures for $Re = 2000$, $Ha = 100$, $h = 1.6$ and spanwise magnetic moment. Four snapshots are shown every 0.8 convective time units which cover one oscillation time of 3.168 time units. (*a*) Top surface with velocity gradient $\partial_z u$. Position of the dipole is indicated with a black dot. The black solid line indicates the line of separation $\partial_z u = 0$. (*b*) Isocontours of $\lambda_2 = -0.5$ at the same time. Direction of view in the picture is the same as in figure 17(*b*).

4.2. *Reynolds number dependence at fixed Hartmann number*

The time-dependent structures are shown in figure 15 for $Re = 2000$ in four snapshots in time intervals of approximately a quarter of the oscillation period. The figure displays the top view of the duct with the position of the dipole marked as a small black dot. The line of separation marks the region of locally reversed flow, i.e. points with $\partial_z u = 0$. Along this line the flow detaches from the surface. This criterion was also used by Mistrangelo (2011) to determine the size of the vortex that occurs in a duct with sudden expansion in dependence on the applied homogeneous magnetic field. There, the magnetic field damps the vortex, in contrast to our investigation with the magnetic field being the source of the vortex formation.

In addition, figure 15 displays the structures in the wake. Here, the presented top surface is coloured with $\partial_z u$. This gradient reaches its maximal value in the Hartmann layers. It should be noted here that the Hartmann layers and the vortex are not completely independent of each other. However, the mechanism that describes the interaction of both, and possibly drives the vortex shedding, has still to be determined.

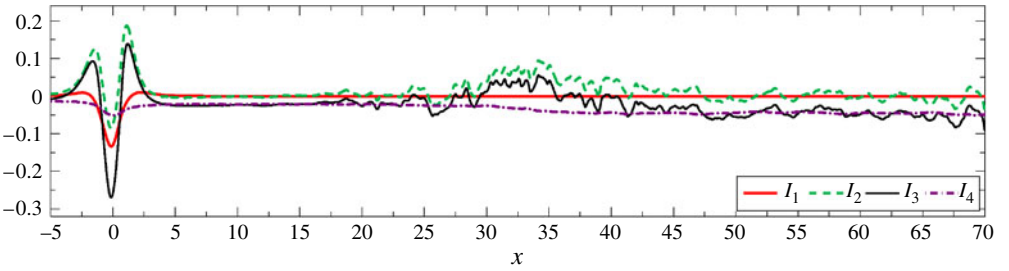

FIGURE 16. (Colour online) Streamwise variation of the different terms of the cross-section averaged momentum balance (3.1) at $Re = 2000$, $Ha = 100$ and $h = 1.6$ for spanwise orientation of the dipole. The data are time-averaged over one period as in figure 12(*b*). The four terms I_1–I_4 are given again by (3.2)–(3.5).

To characterize the three-dimensional structure of the vortices, the λ_2 criterion is used. The pictures on the right-hand side of figure 15 show the isocontours of $\lambda_2 = -0.5$. Each period a hairpin vortex structure is produced. It starts at time $t = 0$ with a small vortex that rotates clockwise about y, i.e. $(\boldsymbol{\nabla} \times \boldsymbol{u})_y > 0$. This vortex is then advected further and surrounded by reversed flow until it passes the position of the dipole at $x = 0$ at time $t = 1/4\,T$, T being the oscillation period. The vortex causes an increase of the width of the area of reversed flow as the back flow has to circumvent the vortex. In parallel, close to the corners of the duct, the Hartmann layer accelerates the flow. The accelerated fluid is blocked by the increase of the width of the reversed flow. This creates two extensions to the vortex at the sides, that are placed at $x = 0$ at time $t = 1/2\,T$. The vortex is then pushed into the bulk away from the top surface (time $t = 3/4\,T$). In this way, the backflow can move freely and recover the high magnitude at the beginning of the area of reversed flow. A next vortex is formed at time $t = T$ and the process repeats. A simple interpretation of this dynamics might therefore be that vortices are produced periodically by roll-up of a shear layer (Kelvin–Helmholtz instability) at the edge of the roughly hemispherical zone shielded by the dipole field from the main flow.

The vortices are transported into the wake and are stretched due to inertia and the shear at the top wall. Thereby, their shape forms into a hairpin-like structure (Davidson 2004). After the hairpin is moved into the wake a new vortex is created by the Lorentz force. Hairpins are well known to appear in vortical shear layers at walls (Jeong *et al.* 1997) and occur in the transition to turbulence in the boundary layer. The spatial development of the wake is determined with the help of the momentum balance (3.1) in figure 16. This figure displays the terms time-averaged over one period T, i.e. it shows the mean of 3168 snapshots at intervals of 0.001 time units, for $Re = 2000$ and $Ha = 100$. The well-pronounced area of distortion with high Lorentz forces in the interval $-5 < x < 5$ is followed by the region of vortex shedding $5 < x < 20$. In this region, the flow is periodic in time with the same frequency as in the area of distortion. Here, the time-averaged momentum balance resembles the laminar flow as the pressure balances the wall stresses and the contribution of the Lorentz force as well as of the momentum flux term are negligibly small. For $x > 25$ this changes to a transitional flow, where the momentum flux term dominates and the wall stresses increase up to a higher constant value as known from turbulent flow. In the beginning of the transitional range, the velocity profiles are found to resemble a turbulent flow but possess a symmetry plane $y = 0$. In this region, large-scale vortices

fill the whole cross-section that break up further downstream. Our time-averaging over one period does not converge in this range because the time-dependence of the structures is non-periodic. Although the computational domain and the calculation time are too short to obtain statistically converged values for the wake, one may expect a fully turbulent flow after a certain transition length. The calculation for $Re = 3000$ indicates that this length decreases for increasing Reynolds number.

In the following, we restrict the study of Reynolds number influence to three exemplary Reynolds numbers: $Re = 1000, 2000$ and 3000 are examined for fixed Hartmann number of $Ha = 100$. The streamlines for the three cases are shown in figure 17. The duct flow is stationary for $Re = 1000$, the wake remains laminar. As for $Re = 2000$, the wake undergoes a transition to turbulence for $Re = 3000$. The vortex structure below the dipole position remains similar for all three cases. The λ_2 criterion reveals here the differences (cf. figure 17*a–c*). For $Re = 1000$ only one vortex is pronounced. In case of $Re \geqslant 2000$, additional vortices are produced in front of the dipole position, at $x < 0$, and during the vortex shedding. The amount and the strength of these vortical structures is enhanced at $Re = 3000$. The principal mechanism of the vortex shedding remains as explained above. The higher the Reynolds number the shorter are the generated hairpin structures in the wake. In addition to the differences in the shape of the flow, the oscillation time is longer with increasing Re. For $Re = 2000$ an oscillation time of 3.168 was calculated, while for $Re = 3000$ it is 3.636 non-dimensional time units. The time signal for both cases is depicted in figure 18.

We conclude from this section that the vortex shedding is a complex mechanism initiated by the Lorentz force. The Reynolds number determines how likely it is that the flow forms vortical structures and transforms into a turbulent flow in the wake. As a final step to this parameter study, it remains to investigate the influence of the Hartmann number on the created vortex.

4.3. *Hartmann number dependence*

To investigate the influence of the Hartmann number, we consider a Reynolds number of 2000 and vary the Hartmann number between 25 and 130. For very small Hartmann number, there is almost no deformation of the flow visible. Figure 19 shows examples of the streamlines for several Hartmann numbers. For $Ha = 25$, one may already observe the local Hartmann layers, but the Lorentz force is not strong enough to create a flow reversal. Such reversed flow is indicated by the streamlines from $Ha = 50$ and higher. A turbulent wake is observed for $Ha \geqslant 80$.

The dependence of the Lorentz force on the Hartmann number is summarized in figure 20. Here, the mean values of the forces are displayed with points and the range of the variation due to the vortex shedding is marked with two bars. Similar to the investigations in § 3, one finds the same power laws for the total forces, i.e. $F_x \sim Ha^2$ and $F_z \sim Ha^4$. The vortex shedding does not influence the power law as the oscillations of F_x and F_z are of the order of 1 and 10 % of the forces, respectively.

As an additional characteristic the frequency of the vortex shedding can be obtained from the time signal of the force. Regarding the dipole as a magnetic obstacle allows one to compare the frequency of vortex shedding with typical values for flows generated past a solid cylinder (see, e.g., Cuevas *et al.* 2006*a*). The non-dimensional parameter for such a comparison would then be the Strouhal number

$$St = \frac{fD}{\bar{u}}. \tag{4.5}$$

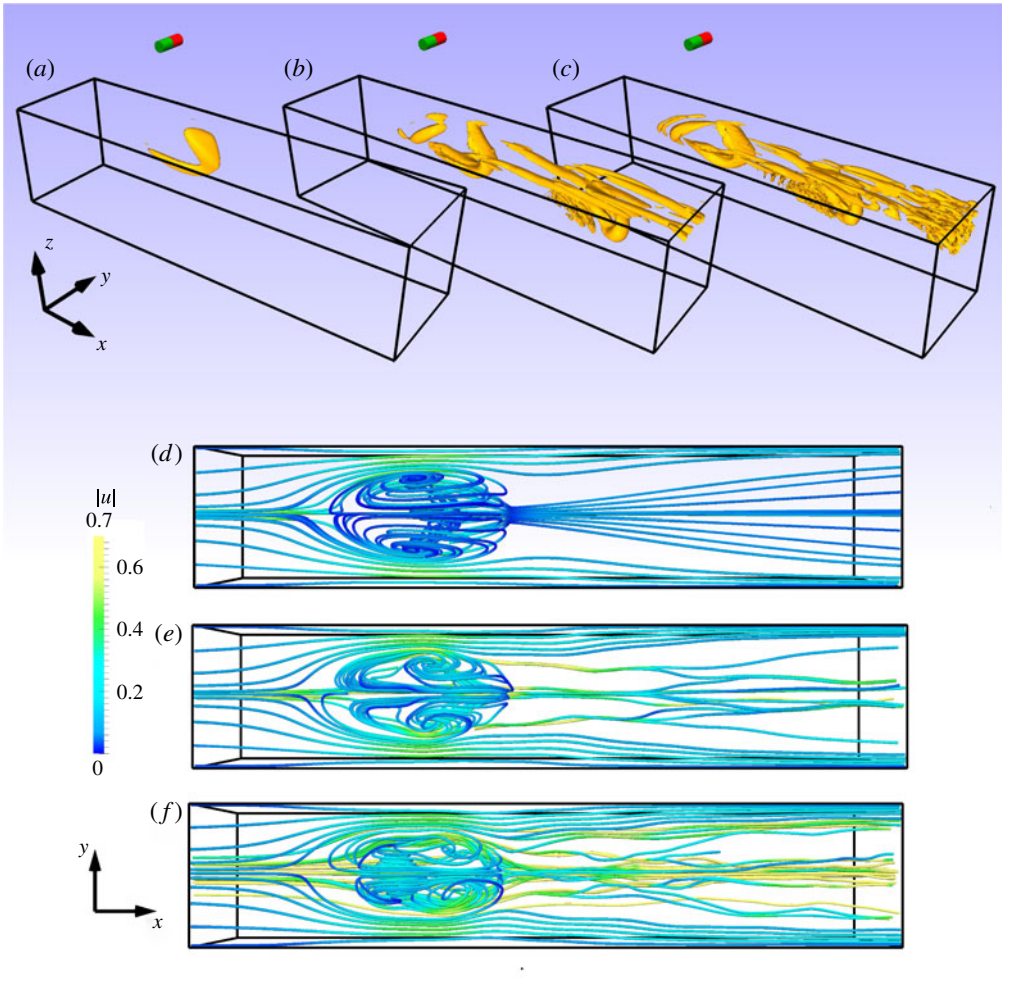

FIGURE 17. (Colour online) Influence of a spanwise oriented dipole on the flow for $Ha = 100$ and $h = 1.6$ at different Reynolds numbers: (*a,d*) $Re = 1000$; (*b,e*) $Re = 2000$; (*c,f*) $Re = 3000$. Snapshots of isocontours of $\lambda_2 = -0.5$ in the range from $x = -3$ to $x = 5$ (*a–c*) and snapshots of streamlines for $x = -3$ to $x = 7$ (*d–f*).

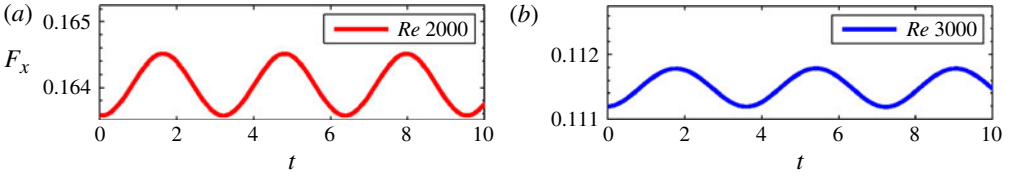

FIGURE 18. (Colour online) Time-dependent behaviour of the force: sinusoidal time signal for (*a*) $Re = 2000$ and (*b*) $Re = 3000$ with $Ha = 100$ and spanwise dipole at a distance of $h = 1.6$.

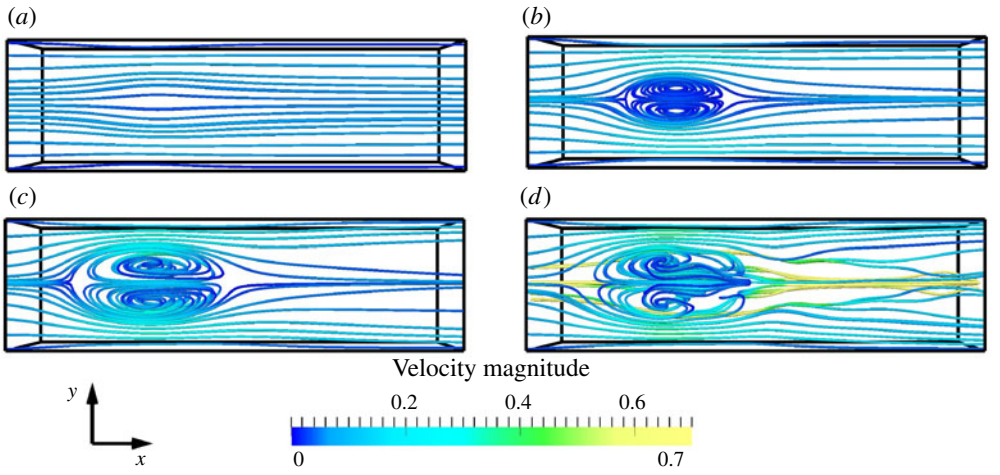

FIGURE 19. (Colour online) Streamlines for different Hartmann numbers and a spanwise dipole orientation at $Re = 2000$ and $h = 1.6$: (*a*) $Ha = 25$; (*b*) $Ha = 50$; (*c*) $Ha = 70$; (*d*) $Ha = 80$. Box indicates the duct from $x = -2$ to $x = 5$. Total length was 15π.

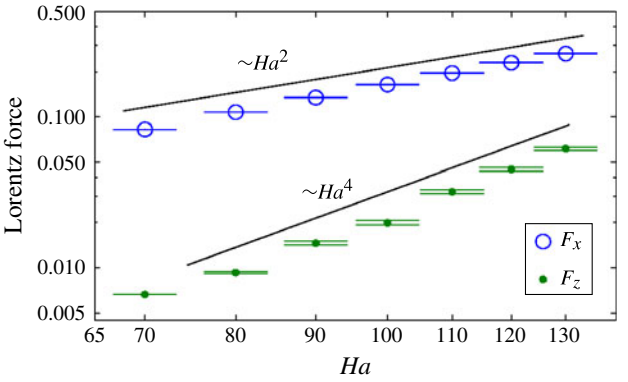

FIGURE 20. (Colour online) Lift and drag forces follow approximately the same power laws as in low Reynolds case (cf. figure 9). Points are given at the mean value while the vertical bars indicate the range of the variation of the time signal.

Here, f denotes the frequency, $\bar{u}$ the mean velocity and D the characteristic length of the obstacle, e.g. the radius of the cylinder. Whereas the frequency and the velocity are known in our setting, it is not obvious how to determine the characteristic length D of the magnetic obstacle. A good estimate for the size of the magnetic obstacle is the area in which the flow is detached from the wall, that was already discussed above (cf. figure 15). This region is stretched along the streamwise direction and the shape may change in time due to the vortex shedding. We define the characteristic length D of the magnetic obstacle as the maximal spanwise width of the area that is enclosed by $\partial_z u_x = 0$ at $z = 1$.

The obtained widths increase with increasing Hartmann number as displayed in figure 21(*a*). In addition, the width is decreased with increasing Reynolds number. It is worth noting the influence of the interaction parameter $N = Ha^2/Re$ in the following

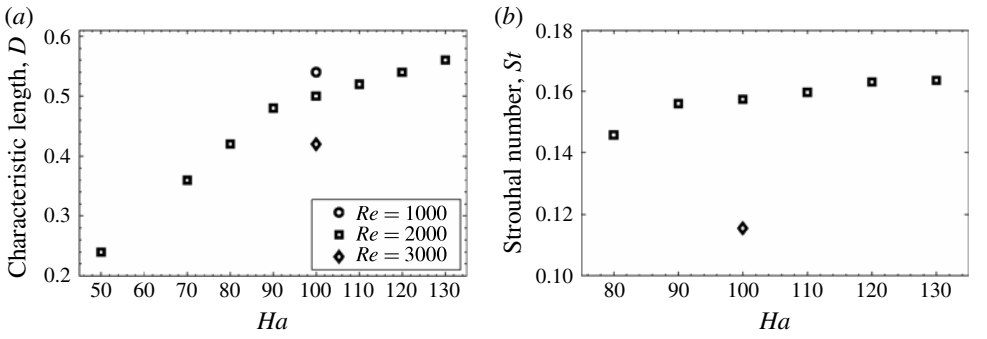

FIGURE 21. Characteristics of the vortex shedding. (*a*) The width of the magnetic obstacle increases linearly for small Hartmann numbers and comes to a saturation for higher *Ha*, where the vortex shedding appears. Increasing the Reynolds number leads to decreased width. (*b*) The Strouhal number increases slightly with increasing Hartmann number and decreases with increasing Reynolds number.

example. The width is approximately the same for the simulations at $Re = 2000$ with $Ha = 80$ and at $Re = 3000$ with $Ha = 100$. Both cases have similar interaction parameters of $N = 3.2$ and $3.\bar{3}$, respectively. This estimate does not hold for the regime without vortex shedding.

Furthermore, the frequency is found to decrease with increasing Hartmann number. This behaviour was also observed for the two-dimensional flow with a small magnetic obstacle (Cuevas *et al.* 2006*a*). The Strouhal number in Cuevas *et al.* (2006*a*) was obtained with a characteristic length that was fixed by the size of the small magnet. Therefore, they describe a decrease of the Strouhal number for increasing Hartmann number with values around $St \sim 0.1$. In a similar parameter study, Kenjeres (2012) found for the same interaction parameters as in our study $St = 0.282$ which is calculated from the power spectra at several positions close to the magnetic obstacle. In the present work, the width of the area of reversed flow is used as a characteristic length of the magnetic obstacle. The width D is therefore a dynamic parameter that depends on *Ha*. If the Hartmann number is enhanced, the resulting Strouhal number increases with a gentle slope and reaches a saturation around $St \sim 0.16$ (cf. figure 21*b* for $Re = 2000$).

The result can be compared with the flow around a solid cylinder. There, the Strouhal number is of the order $St \sim 0.2$ (Williamson 1996). Dousset & Pothérat (2008) investigated the influence of a homogeneous magnetic field on the flow around a cylinder. In the regime of high Reynolds number, the Strouhal number was found to decrease with increasing Hartmann number. Thus, the homogeneous magnetic field damps the vortical structures. In our case, the inhomogeneous localized magnetic field gives rise to the vortex formation and subsequent shedding.

Apart from the Strouhal number, it is desirable to have an additional quantity for the deflection of the flow that is caused by the dipole. The aim is therefore to characterize the structures in figure 19. A possible approach is to measure the vorticity, $\boldsymbol{\omega} = \nabla \times \boldsymbol{u}$, of the flow. For this, we consider the enstrophy over a duct fraction right below the dipole which is defined as

$$\Omega = \int_{[-1,1]^3} \frac{1}{2} |\nabla \times \boldsymbol{u}|^2 \, \mathrm{d}V. \tag{4.6}$$

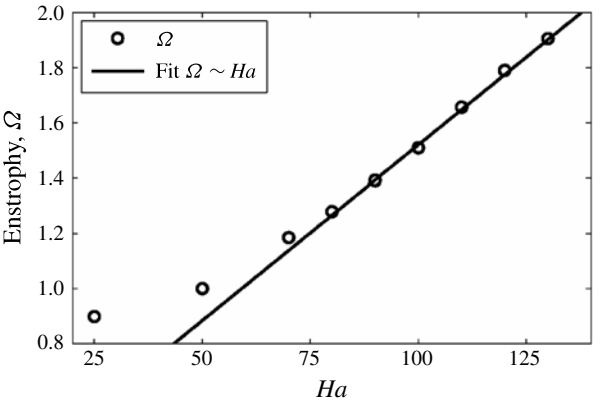

FIGURE 22. The total enstrophy Ω as calculated in (4.6) is linear dependent on the Hartmann number. This behaviour is originated in the local Hartmann layers. Data is given for $Re = 2000$, $h = 1.6$ and spanwise-oriented dipole.

As the wake contains turbulent vortices, the integral is not applied to the whole domain. Thus, we focus on the area that is directly influenced by the dipole. Figure 22 shows that the enstrophy increases linearly with the Hartmann number, which is caused by an increase of the vorticity $\boldsymbol{\omega} = \boldsymbol{\nabla} \times \boldsymbol{u}$ in the vortex as well as the Hartmann layers. The strongest contribution comes from the partial derivative $\partial_z u_x$, which reaches maximal magnitudes in the Hartmann layer, as already mentioned above (cf. figure 15). An integration shows that the integral $\int_{[-1,1]^3} |\partial_z u_x|^2 \, \mathrm{d}V/2$ gives already about 80 % of the magnitude of the total enstrophy Ω.

To explain the linear dependence on the Hartmann number, we recall the properties of the Hartmann layers in homogeneous magnetic fields. It is known from the analytic solution of the Hartmann channel flow (Müller & Bühler 2001) that $u_x \sim 1 - \exp(-Ha\, z)$, where z measures the distance from the wall. We can therefore estimate $(\partial_z u_x)^2 \sim (Ha \exp(-Ha\, z))^2$ in the Hartmann layer. The width of the Hartmann layer is given by $\delta \sim 1/Ha$. Therefore, the integration of the enstrophy leads to $\Omega \sim \int_0^\delta |(\partial_z u_x)^2| \, \mathrm{d}z \sim Ha$.

It has to be remarked here that this explanation is only valid for the total enstrophy of duct flow in a uniform magnetic field when Ha is large. While the Hartmann layers show linear dependence of the total enstrophy on the Hartmann number, there are additional contributions from the Shercliff layers proportional to $Ha^{1/2}$. As a conclusion, the qualitative presentation of the flow structures in terms of the enstrophy (4.6) fails to provide details on the reversed flow and the vortex structures. Nevertheless, it gives a good criterion for the strength of the local Hartmann layers.

5. Conclusion and outlook

In this work, we have investigated the influence of a localized inhomogeneous magnetic field on liquid metal flow in the quasistatic approximation. Our study focuses on the fundamental aspects of the structure formation. Therefore, we use the simplest setting, a point dipole for the *localized* magnetic field and a simple shear flow in a square duct. It should therefore be considered as a paradigm for many realistic liquid metal flows. The magnetic field gives rise to a Lorentz force in the liquid that deforms the streamlines. Depending on the orientation of the dipole, areas of reversed flow and

localized or local Hartmann layers are formed at the top surface due to strong Lorentz forces. The notion of local Hartmann layer is considered as a generalization of the canonical Hartmann flow and layer which arises due to the finite spanwise extension in the square cross-section of the duct and the locality of the magnetic field. We have provided a systematic parameter dependence study which unravelled the local effects of the dipole field on the flow.

The parameter study is focused on the influence of the Reynolds and the Hartmann number. As expected the flow remains laminar and stationary for low Reynolds numbers. When the Reynolds number is increased, we observe that the length of the wake is increased. We showed that the spatial downstream decay rate of the deflected flow in the wake is proportional to $1/Re$. For $Re \geqslant 2000$, the spanwise-oriented dipole in a distance of $h = 1.6$ triggers vortex shedding in case of Hartmann number above 80. The flow becomes time-dependent and eventually turbulent.

The Hartmann number affects the total Lorentz force. The drag component is proportional to Ha^2, while the lift force behaves like Ha^4 for $Ha \leqslant 25$. The latter is connected with the nonlinearity in the Navier–Stokes equation. In the case of time-dependent flow with a spanwise oriented dipole, the vortex shedding leads to a sinusoidal force signal. The frequency of the signal corresponds to a Strouhal number that increases with increasing Hartmann number. The Strouhal number saturates around 0.16 which is comparable with classical flow past a cylinder. Nevertheless, it is not only the primary vortex, that has strong influence of the flow structure, but also the local Hartmann layers. Owing to the formation of these boundary layers, the enstrophy of the deformed flow increases linearly with the Hartmann number.

Our study opens some new perspectives for flow manipulation and thus also for flow control. The described setting can be used to trigger turbulence in a laminar flow. This can be applied, e.g., for mixing injected substances or particles with the main flow. Such applications as well as experimental investigations of the problem have to be performed with magnetic fields that are localized and inhomogeneous but not necessarily of the shape of a point dipole. Future numerical studies should include a turbulent inflow to model the experimental setting more realistically.

To obtain a complete understanding of the mechanism of the vortex shedding, the stability study can be extended. This could be provided by adding prescribed perturbations to a deformed but stationary flow. A more sophisticated way would be the direct optimal growth analysis as used by Barkley, Blackburn & Sherwin (2008) or a sensitivity study such as that performed by Giannetti & Luchini (2007).

Finally, the study should be extended to capture the influence of geometry parameters such as the distance of the dipole or its orientation. Here, the question arises whether the vortex shedding is still present if the dipole is oriented in an oblique orientation and what the optimal local Hartmann layers are to trigger flow transition. In addition, the symmetry of the given setting could be broken if the dipole is not positioned in the centreline of the duct, but with a certain offset. The influences of walls could also be studied by using rectangular ducts with non-square cross-section or pipes. These investigations open a huge parameter space that has to be considered in future works.

Acknowledgements

The authors wish to thank D. Krasnov for providing the core of the numerical code used and for many fruitful discussions. We have also benefited from discussions with O. Zikanov, A. Thess and B. Knaepen. The authors gratefully acknowledge the

financial support from the Deutsche Forschungsgemeinschaft in the framework of the Research Training Group Lorentz force velocimetry and Lorentz force eddy current testing (grant DFG GK 1567/1). The numerical calculations have been performed on the cluster at TU Ilmenau and on the Juropa cluster at NIC/JSC (Jülich).

REFERENCES

ADAMS, J. C., SWARZTRAUBER, P. & SWEET, R. 1999 Efficient Fortran subprograms for the solution of separable elliptic partial differential equations. http://www.cisl.ucar.edu/css/software/fishpack/.

AIRIAU, C. & CASTETS, M. 2004 On the amplification of small disturbances in a channel flow with normal magnetic field. *Phys. Fluids* **16** (8), 082991.

ALBOUSSIÉRE, T. 2001 Quasi characteristic MHD flows. *C. R. Acad. Sci. Paris. Ser. IIB – Mechanics* **329** (10), 767–773.

ALBOUSSIÉRE, T., GARANDET, J. P. & MOREAU, R. 1996 Asymptotic analysis and symmetry in MHD convection. *Phys. Fluids* **8** (8), 082215.

ALBRECHT, T., GRUNDMANN, R., MUTSCHKE, G. & GERBETH, G. 2006 On the stability of the boundary layer subject to a wall-parallel Lorentz force. *Phys. Fluids* **18** (9), 098103.

ANDREEV, O., KOLESNIKOV, Y. & THESS, A. 2006 Experimental study of liquid metal channel flow under the influence of a non-uniform magnetic field. *Phys. Fluids* **18** (6), 065108.

ANDREEV, O., KOLESNIKOV, Y. & THESS, A. 2009 Application of the ultrasonic velocity profile method to the mapping of liquid metal flows under the influence of a non-uniform magnetic field. *Exp. Fluids* **46**, 77–83.

BARKLEY, D., BLACKBURN, H. M. & SHERWIN, S. J. 2008 Direct optimal growth analysis for time steppers. *Intl J. Numer. Meth. Fluids* **57**, 1435–1458.

BISKAMP, D. 1993 *Nonlinear Magnetohydrodynamics*. Cambridge University Press.

BOECK, T., KRASNOV, D. & ZIENICKE, E. 2007 Numerical study of turbulent magnetohydrodynamic channel flow. *J. Fluid Mech.* **572**, 179–188.

CHAUDHARY, R., VANKA, S. P. & THOMAS, B. G. 2010 Direct numerical simulations of magnetic fields on turbulent flow in a square duct. *Phys. Fluids* **22** (7), 075102.

CUEVAS, S., SMOLENTSEV, S. & ABDOU, M. A. 2006*a* On the flow past a magnetic obstacle. *J. Fluid Mech.* **553**, 227–252.

CUEVAS, S., SMOLENTSEV, S. & ABDOU, M. A. 2006*b* Vorticity generation in creeping flow past a magnetic obstacle. *Phys. Rev.* E **74** (5), 1–10.

DAVIDSON, P. A. 1999 Magnetohydrodynamics in material processing. *Annu. Rev. Fluid Mech.* **31**, 273–300.

DAVIDSON, P. A. 2004 *Turbulence: An Introduction for Scientists and Engineers*. Oxford University Press.

DAVIDSON, P. A. (Ed.) 2006 *An Introduction to Magnetohydrodynamics*. Cambridge University Press.

DOUSSET, V. & POTHÉRAT, A. 2008 Numerical simulations of a cylinder wake under a strong axial magnetic field. *Phys. Fluids* **20** (1), 017104.

GAVRILAKIS, S. 1992 Numerical simulation of low-Reynolds-number turbulent flow through a straight square duct. *J. Fluid Mech.* **244**, 101–129.

GERARD-VARET, D. 2002 Amplification of small perturbations in a Hartmann layer. *Phys. Fluids* **14** (4), 1458–1467.

GIANNETTI, F. & LUCHINI, P. 2007 Structural sensitivity of the instability of the cylinder wake. *J. Fluid Mech.* **581**, 167–197.

HARTMANN, J. 1937 Hg-dynamics I. Theory of the laminar flow of an electrically conductive liquid in a homogeneous magnetic field. *K. Dan. Vidensk. Selsk. Mat. Fys. Medd.* **15** (6), 1–28.

HARTMANN, J. & LAZARUS, F. 1937 Hg-dynamics II. Experimental investigations on the flow of mercury in a homogeneous magnetic field. *K. Dan. Vidensk. Selsk. Mat. Fys. Medd.* **15** (7), 1–45.

HEINICKE, C. 2013 Spatially resolved measurements in a liquid metal OW with Lorentz force velocimetry. *Exp. Fluids* **54** (6) 1560, 1–8.

HEINICKE, C., TYMPEL, S., PULUGUNDLA, G., RAHNEBERG, I., BOECK, T. & THESS, A. 2012 Interaction of a small permanent magnet with a liquid metal duct flow. *J. Appl. Phys.* **112** (12), 124914.

HUSER, A. & BIRINGEN, S. 1993 Direct numerical simulation of turbulent flow in a square duct. *J. Fluid Mech.* **257**, 65–95.

JACKSON, J. D. 1998 *Classical Electrodynamics*, 3rd edn. Wiley.

JEONG, J. & HUSSAIN, F. 1995 On the identification of a vortex. *J. Fluid Mech.* **285**, 69–94.

JEONG, J., HUSSAIN, F., SCHOPPA, W. & KIM, J. 1997 Coherent structures near the wall in a turbulent channel flow. *J. Fluid Mech.* **332**, 185–214.

KENJERES, S. 2012 Energy spectra and turbulence generation in the wake of magnetic obstacle. *Phys. Fluids* **24** (11), 115111.

KNAEPEN, B. & MOREAU, R. 2008 Magnetohydrodynamic turbulence at low magnetic Reynolds number. *Annu. Rev. Fluid Mech.* **40**, 25–45.

KOBAYASHI, H. 2008 Large eddy simulation of magnetohydrodynamic turbulent duct flows. *Phys. Fluids* **20** (1), 015102.

KRASNOV, D., THESS, A., BOECK, T., ZHAO, Y. & ZIKANOV, O. 2013 Patterned turbulence in liquid metal flow: computational reconstruction of the Hartmann experiment. *Phys. Rev. Lett.* **110** (8), 084501.

KRASNOV, D., ZIKANOV, O. & BOECK, T. 2011 Comparative study of finite difference approaches in simulation of magnetohydrodynamic turbulence at low magnetic Reynolds number. *Comput. Fluids* **50** (1), 46–59.

KRASNOV, D., ZIKANOV, O. & BOECK, T. 2012 Numerical study of magnetohydrodynamic duct flow at high Reynolds and Hartmann numbers. *J. Fluid Mech.* **704**, 421–446.

KRASNOV, D., ZIKANOV, O., ROSSI, M. & BOECK, T. 2010 Optimal linear growth in magnetohydrodynamic duct flow. *J. Fluid Mech.* **653**, 273–299.

KRASNOV, D. S., ZIENICKE, E., ZIKANOV, O., BOECK, T. & THESS, A. 2004 Numerical study of the instability of the Hartmann layer. *J. Fluid Mech.* **504** (2004), 183–211.

KULIKOVSKII, A. G. 1968 Slow steady flow of a conducting liquid at large Hartmann numbers. *Izv. Akad. Nauk SSSR Mekh. Zhidk. Gaza* **3** (2), 3–10.

MISTRANGELO, C. 2011 Topological analysis of separation phenomena in liquid metal flow in sudden expansions. Part 2. Magnetohydrodynamic flow. *J. Fluid Mech.* **674**, 132–162.

MOREAU, R. J. 1990 *Magnetohydrodynamics*. Kluwer.

MORINISHI, Y., LUND, T. S., VASILYEV, O. V. & MOIN, P. 1998 Fully conservative higher-order finite difference scheme for incompressible flow. *J. Comput. Phys.* **143** (1), 90–124.

MÜLLER, U. & BÜHLER, L. 2001 *Magnetohydrodynamics in Channels and Containers*. Springer.

NI, M.-J., MUNIPALLI, R., MORLEY, N. B., HUANG, P. & ABDOU, M. A. 2007 A current density conservative scheme for incompressible MHD flows at low magnetic Reynolds number. Part I. On a rectangular collocated grid system. *J. Comput. Phys.* **227**, 174–204.

NIU, K. 1989 *Nuclear Fusion*. Cambridge University Press.

NORDSTRÖM, J., NORDIN, N. & HENNINGSON, D. 1999 The fringe region technique and the Fourier method used in the direct numerical simulation of spatially evolving viscous flows. *SIAM J. Sci. Comput.* **20** (4), 1365–1393.

POZRIKIDIS, C. (Ed.) 1997 *Introduction to Theoretical and Computational Fluid Dynamics*. Oxford University Press.

PRIEDE, J., BUCHENAU, D. & GERBETH, G. 2011 Single-magnet rotary flowmeter for liquid metals. *J. Appl. Phys.* **110** (3), 034512.

RÜDIGER, G. & HOLLERBACH, R. 2004 *The Magnetic Universe: Geophysical and Astrophysical Dynamo Theory*. Wiley-VCH.

SHATROV, V. & GERBETH, G. 2010 Marginal turbulent magnetohydrodynamic flow in a square duct. *Phys. Fluids* **8** (5), 084101.

SHERCLIFF, J. A. (Ed.) 1962 *The Theory of Electromagnetic Flow Measurement*. Cambridge University Press.

SHERCLIFF, J. A. (Ed.) 1965 *A Textbook of Magnetohydrodynamics*. Pergamon.

SIMENS, M. P., JIMÉNEZ, J., HOYAS, S. & MIZUNO, Y. 2009 A high-resolution code for turbulent boundary layers. *J. Comput. Phys.* **228**, 4218–4231.

STEFANI, F., GUNDRUM, T. & GERBETH, G. 2004 Contactless inductive flow tomography. *Phys. Rev.* E **70** (5), 056306.

THESS, A., VOTYAKOV, E., KNAEPEN, B. & ZIKANOV, O. 2007 Theory of the Lorentz force flowmeter. *New J. Phys.* **9** (8) 299, 1–27.

THESS, A., VOTYAKOV, E. & KOLESNIKOV, Y. 2006 Lorentz force velocimetry. *Phys. Rev. Lett.* **96** (16), 164501.

TYMPEL, S. 2013 Magnetohydrodynamic duct flow in the presence of a magnetic dipole. PhD thesis, Ilmenau University of Tehcnology, Germany, http://www.db-thueringen.de/servlets/DocumentServlet?id=22327.

TYMPEL, S., KRASNOV, D., BOECK, T. & SCHUMACHER, J. 2012 Distortion of liquid metal flow in a square duct due to the influence of a magnetic point dipole. *Proc. Appl. Maths Mech.* **12** (1), 567–568.

UHLMANN, M. & NAGATA, M. 2006 Linear stability of flow in an internally heated rectangular duct. *J. Fluid Mech.* **551**, 387–404.

VANTIEGHEM, S., ALBETS-CHICO, X. & KNAEPEN, B. 2009 The velocity profile of laminar MHD flows in circular conducting pipes. *Theor. Comput. Fluid Dyn.* **23** (6), 525–533.

VOTYAKOV, E., KOLESNIKOV, Y., ANDREEV, O., ZIENICKE, E. & THESS, A. 2007 Structure of the wake of a magnetic obstacle. *Phys. Rev. Lett.* **98** (14), 144504.

VOTYAKOV, E., ZIENICKE, E. & KOLESNIKOV, Y. 2008 Constrained flow around a magnetic obstacle. *J. Fluid Mech.* **610**, 131–156.

WILLIAMSON, C. K. H. 1996 Vortex dynamics in the cylinder wake. *Annu. Rev. Fluid Mech.* **28**, 477–539.

ZHAO, Y. & ZIKANOV, O. 2012 Instabilities and turbulence in magnetohydrodynamic flow in a toroidal duct prior to transition in Hartmann layers. *J. Fluid Mech.* **692**, 288–316.